Correlation between unsteady-state solidification thermal parameters and microstructural growth of Zn–8 mass% Al and Zn–8 mass% Al–XBi tribological alloys

Rudimylla S. Septimio[1] · Thiago A. Costa[2] · Cássio A. P. Silva[3] · Talita A. Vida[4] · Juan de Damborenea[5] · Amauri Garcia[4] · Noé Cheung[4]

Abstract

In the present study, directionally solidification experiments are performed with Zn–8 mass% Al and Zn–8 mass% Al–X mass% Bi (X=1.5, 2.3 and 3.0 mass%) alloys using a water-cooled solidification system, which permits a wide range of solidification cooling rates to be investigated in a single experiment. The microstructural phases of the ternary alloys are shown to be quite similar to those of the binary alloy, with equiaxed dendrites immersed in a matrix formed by fibers or lamellae of the Al/Zn eutectoid product, with the difference that the ternary alloys have Bi droplets disseminated into the matrix and dendrite branches. The dendrites, lamellae and fibers evolve from a refined microstructure at regions closer to the water-cooled bottom of the casting, to increasingly coarser microstructures toward the top. Experimental expressions relating the secondary dendritic arm spacing, the spacing between lamellae and the fiber spacing to solidification thermal parameters (growth and cooling rates) are derived. For the alloys having higher Bi content, a bimodal distribution of Bi droplets was shown to occur, with small droplets, consisting of lamellae and fibers, disseminated into the matrix and larger droplets between the dendritic branches.

Keywords Zn–Al–(Bi) alloys · Solidification · Thermal parameters · Microstructure

Introduction

Zn–Al-based alloys represent a group of tribological materials qualified for the manufacture of bearings. They have been extensively studied as they are the base of

✉ Noé Cheung
cheung@fem.unicamp.br

[1] Institute of Geosciences and Engineering, Federal University of the South and Southeast of Pará, UNIFESSPA, Marabá, PA 68050-080, Brazil

[2] Federal Institute of Education, Science and Technology of Pará, IFPA, Belém, PA 66093-020, Brazil

[3] Federal University of São Paulo, UNIFESP, São José dos Campos, SP 12231-280, Brazil

[4] Department of Manufacturing and Materials Engineering, University of Campinas, UNICAMP, Campinas, SP 13083-860, Brazil

[5] National Center for Metallurgical Research, CENIM-CSIC, 28040 Madrid, Spain

commercial alloys known as ZA (zinc–aluminum), which have small additions of copper and magnesium. Commercial designations such as ZA-8, ZA-12 and ZA-27 are based on aluminum contents of 8, 12 and 27 mass%, respectively. Zn–Al alloys have good mechanical strength and hardness and are widely used in the manufacture of bearings because of their good wear resistance [1–3].

Controlling the microstructure through solidification thermal parameters is of critical importance since it plays an important role on mechanical properties, corrosion behavior and also on wear resistance of metallic alloys. Several experimental investigations are reported in the literature relating solidification thermal parameters to microstructure features [4–8]. Osório et al. [9] investigated the influence of heat transfer on the as-solidified microstructures of Zn–X mass% Al (1, 3 and 4 mass% Al) alloys and their correlation with tensile properties. The experimental results included: transient metal/mold heat transfer coefficients, secondary dendrite arm spacings and ultimate and yield tensile strengths as a function of

solidification conditions imposed by the metal/mold system. The results emphasized the role of the microstructural arrangement, which is governed by thermal parameters, on the resulting mechanical properties. Experimental expressions correlating tensile properties with a representative scale of the microstructure have proved to be a promising tool in the preprogramming of solidification conditions in the casting process, with a view to permitting a required mechanical strength to be achieved. Another study focused on the influence of the as-cast dendritic microstructure of a Zn–27 mass% Al alloy on the tensile properties, which permitted experimental expressions correlating the ultimate tensile and yield strengths with the secondary dendrite arm spacing to be derived. These results showed that both tensile properties increase with decreasing dendrite spacings [10].

Pizarro Pastene et al. [11] studied Zn–Al alloys having different Al contents (0.5, 2, 4 and 8 mass% Al), which were directionally grown in a Bridgman device aiming to understand the formation of microstructures under different solidification paths. The hypoeutectic Zn–0.5 mass% Al was reported to have a microstructure characterized by cellular and dendritic morphologies, while the proeutectic alloys (2 and 4 mass% Al) presented a dendritic primary phase surrounded by the eutectic mixture, without apparent interaction. The hypereutectic Zn–8 mass% Al alloy was shown to grow in a similar way to that of the proeutectic alloys, except for the primary phase that in this case is an Al-rich phase.

The addition of alloying elements to Zn–Al alloys with a view to improving the resulting mechanical properties has been used in many studies. Since Zn–Al alloys present poor lubrication, Türk et al. [1] analyzed the additions of 1 mass% of Pb, Sn and Cd to compensate for this deficiency. The wear tests performed showed that for a 30-N load, the best wear resistance was associated with the ZA8 alloy with addition of Pb and for a higher load (45 N) with the ZA8 alloy with addition of Cd. The addition of Sn was shown to be the worst option for both analyzed load tests. It is worth noting that Pb and Cd are now being banned due to the risks to health and environmental contamination, which means that there is a need for new alloys options having a phase that fulfills the role of lubricant.

Other studies in the literature also focus on the addition of a third element to Zn–Al alloys such as, Ag [2], Cu [3] [12], Si [13] and even Al_2O_3 particles [14]. Like Al-based monotectic alloys, for which Bi dispersed in the matrix acts as a self-lubricant agent, Zn–Al–Bi alloys that have been scarcely explored in the literature, may also have good potential for promising applications in automotive components that require wear resistance. Bi particles well distributed through the alloy microstructure may flow easily under sliding conditions, resulting in favorable

tribological performance [15]. The amount, shape and arrangement of microstructural features are particularly important from the point of view of wear behavior, that is, a stronger comprehension on how the alloy microstructure evolves during solidification is necessary.

The addition of Bi can give rise to immiscible alloys systems characterized by monotectic reactions. Monotectic systems consist of elements with different physical properties that cover a certain composition range giving rise to a miscibility gap. At the monotectic temperature, the homogeneous liquid L′, which contains the alloy components A and B, transforms into an A-rich solid α and a B-rich liquid L″ simultaneously through the monotectic reaction (L′=α+L″) [16]. Even with the elements A and B being almost insoluble in each other in the solid state, the resulting alloy has properties combining characteristics of both elements, which can generate novel materials with exceptional functional properties distinct than those for which each phase is taken separately [17]. Consequently, the microstructure of monotectic alloys offers several possibilities for the development of new alloys for technological applications, such as self-lubricant bearings [18]. However, systematic studies on the evolution of ternary monotectic alloys are still scarce in the literature, mainly under transient solidification regimes, which encompasses most industrial conditions.

Generally, monotectic alloy systems present quite simple phase diagrams with monovariant three-phase equilibrium, L′+L″+Solid, as in the Al–Bi–Pb, Al–Bi–In and Al–Pb–In alloys systems [19]. However, some ternary systems may act differently presenting four-phase equilibrium, L′+L″+Solid 1+Solid 2 [20]. Therefore, completely different microstructures with higher level of complexity can be expected. Djordje Mirković et al. [21] studied the solidification paths of the Al–Bi–Zn alloy system using thermodynamic calculations, as well as the resulting microstructure of samples solidified at a cooling rate of 1 K min⁻¹. It was noticed that the liquid gap L′+L″ intersects the primary crystallization fields of Al and Zn, giving rise to the four-phase reaction. In other words, the transformation L′=L″+(Al)′+(Zn)′ may be the combined result of the binary reactions L′=L″+(Al) at 658 °C from the Al–Bi system and L′=L″+(Zn) at 416 °C from the Bi–Zn system. The cross section microstructures of alloys samples confirmed the phase separation into large cohesive and rounded regions during cooling. These two different regions: Bi-poor liquid (L′) and Bi-rich liquid (L″), were clearly seen in electron micrographs of as-solidified samples. The presence of tiny droplets of Bi-rich L″ within L″+ (Al)+(Zn) areas eventually solidified as a result from the demixing stage of the two liquids.

Although there are some studies in the literature related to the addition of Bi in Zn–Al alloys [20, 21], there is a

lack of systematic investigations on the microstructural evolution of both Zn–Al and Zn–Al–Bi alloys, connected to the experimental thermal parameters under transient solidification conditions. It is well known that the microstructure of metallic components depends strongly on the parameters of their manufacturing route and depending on the cooling conditions during solidification in the casting process, the resulting microstructural phases may be entirely dissimilar from those settled by the corresponding equilibrium phase diagram [22, 23]. The purpose of this study is to perform directionally solidification experiments with Zn–Al and Zn–Al–Bi alloys using a water-cooled solidification system, in which a wide range of cooling rates can be investigated in a single experiment, thus permitting the corresponding microstructural development to be investigated. The solidification thermal parameters (growth rate, V, and cooling rate, $\dot{T}$) will be determined with a view to establishing experimental relationships between representative length scales of the phases forming the microstructure and both V and $\dot{T}$. Particularly inherent of the aforementioned alloys systems, the resulting microstructures are characterized by a series of morphological features related to invariant reactions (monotectic, eutectoid and eutectic) such as, dendrites, lamellae, fibers and droplets. The present work aims to contribute to a better understanding on the arrangement of these features during the cooling process, envisaging future correlations with the wear behavior of these tribological alloys.

Experimental

The solidification setup, shown in Fig. 1, permits the alloy to be melted in situ and enables the unidirectional transient solidifi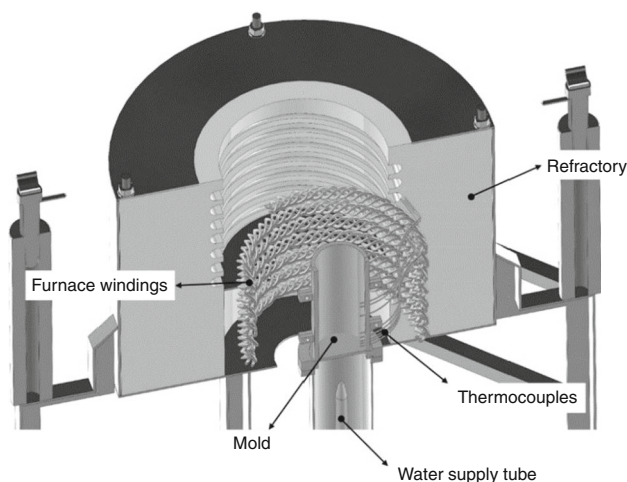cation of castings to be produced by extracting heat through a water-cooled mold bottom. The lateral inner surface of a stainless-steel split mold (internal diameter of 56 mm, a height of 80 mm and a wall thickness of 10 mm) is covered with a layer of insulating alumina to minimize radial heat losses. The mold is positioned at the center of the solidification apparatus, and to reduce heat losses from the metal/air surface, a top cover made of an insulation material is also used. Heat is directionally extracted only through the water-cooled mold bottom made of low carbon steel (3 mm thick and polished with 100, 200, 400, 600 and 1200 grit SiC papers), permitting a wide range of solidification cooling rates to be operative along the length of the directionally solidified (DS) casting.

The solidification experiments were carried out with four different alloys compositions: Zn–8 mass% Al; Zn–8 mass% Al–1.5 mass% Bi; Zn–8 mass% Al–2.3 mass% Bi; and Zn–8 mass% Al–3.0 mass% Bi. Figure 2 shows the partial binary Zn–Al phase diagram, where the Zn–8 mass % Al alloy is indicated by a vertical line. Figure 3 shows the pseudo-binary diagram Zn–8 mass% Al–Bi with the analyzed alloys indicated at the right side by vertical lines. Both phase diagrams were calculated by the ThermoCalc software.

The alloys were prepared by melting weighed quantities of Zn, Al and Bi of high purity (>99%) in a graphite crucible in a muffle furnace. The chemical compositions of all elements used to prepare the alloys are shown in Table 1. Firstly, Zn and Al were melted together and for the alloys containing Bi, pieces of Bi were added to the molten
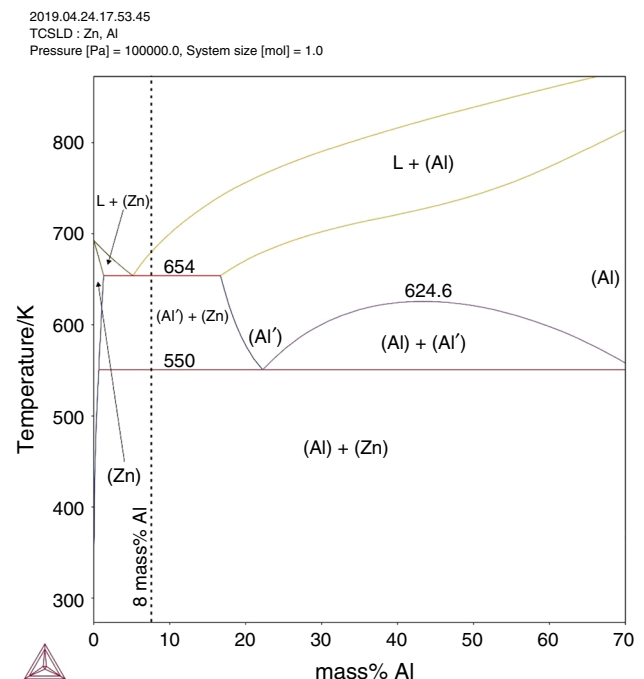

Fig. 1 Schematics of the vertical upward directional solidification setup

Fig. 2 Partial Zn–Al binary phase diagram. (ThermoCalc)

2019.04.24.17.51.14
TCSLD3 : Zn, Al, Bi
Pressure [pa] = 100000.0, System size [mol] = 1.0, Mass percent Al = 8.0

2019.04.24.17.47.29
TCSLD3 : Zn,Al, Bi
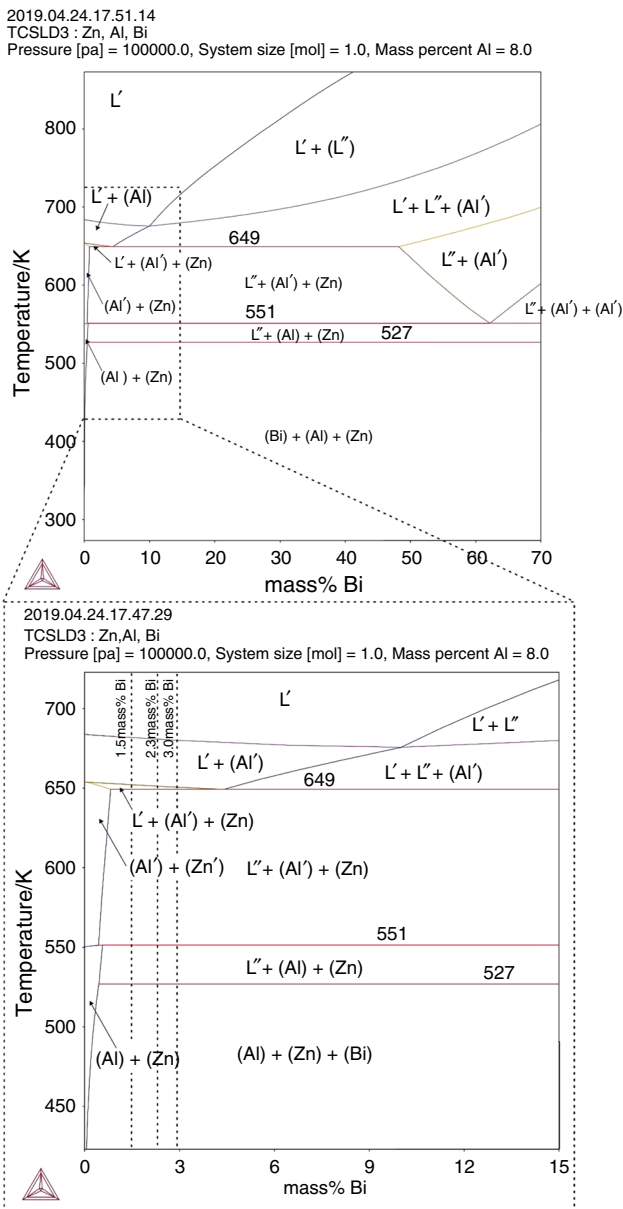Pressure [pa] = 100000.0, System size [mol] = 1.0, Mass percent Al = 8.0

Fig. 3 Partial Zn–8 mass% Al–Bi pseudo-binary phase diagram with vertical lines indicating the analyzed alloys compositions (ThermoCalc)

liquid. In the sequence, to guarantee homogenization, the resulting mixture was mechanically agitated with a stainless-steel bar covered with a layer of insulating alumina, in order to avoid iron contamination. The molten alloy was then poured into the casting chamber of the directional

solidification apparatus, in which the alloy was remelted in presence of argon flow injected into the casting chamber in order to generate a protective atmosphere. Subsequently, the electric heaters were disconnected and as soon as the temperature stabilized at 10% above the liquidus temperature, the water flow was initiated at the bottom part of the mold, allowing the onset of solidification.

A bank of fine type K thermocouples (±0.4% uncertainty), positioned at eight different locations from the heat-extracting surface at the bottom of the DS casting, along its center line, was used to monitor the temperature evolution during solidification. All thermocouples were connected by coaxial cables to a data logger of 12 bits interfaced with a computer, and the temperature data were acquired automatically at a frequency of 5 Hz. The positions of the thermocouple's tips can vary from an experiment to another during some experimental steps, such as thermocouple placement procedure, initial pouring of the molten alloy into the mold cavity and injection of argon into the casting chamber. Hence, postmortem examination of each DS casting was carried out with a view to determining more accurately each thermocouple position.

In order to reveal the macrostructure, the cylindrical castings were subsequently sectioned along their vertical axes, grounded and etched with the Poulton's reagent (HF, HCl, HNO_3 and water). Samples were extracted from different sections (longitudinal and transversal) along the length of each DS casting, as shown in Fig. 4, with a view to permitting the microstructure evolution from the base to the top of the casting to be characterized. The samples were polished with 100, 200, 400, 600 and 1200 grit SiC papers, and then finely polished with diamond paste (6 and 1 μm). No etching was necessary for revealing the microstructure of the samples.

The examination of microstructures was carried out using an optical Olympus inverted metallurgical microscope (model 41 GX) and backscattered electron imaging (BSE) of scanning electron microscopes (SEM Shimadzu, VEGA 3 SBU TESCAM and SEM Zeiss model Evo MA15). An energy dispersive spectrometer (EDS AZTec Energy X-Act, Oxford) was used to complement the microstructural characterization. In addition, X-ray diffraction analyses were performed using a Siemens D5000 diffractometer, with Cu-Kα target X-ray tubes and radiation with wavelength equal to 1.54 Å. The Rietveld method was applied to quantify the detected phases.

Table 1 Chemical composition/mass% of metals used to prepare the alloys

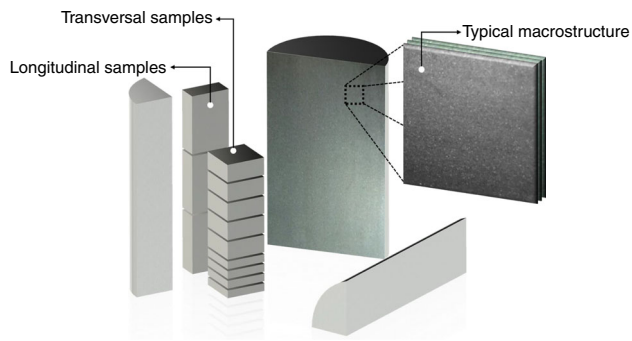| Elem	Bi	Zn	Al	Ag	Sn	Fe	Cd	Pb	Si	Mg	Cu
Bi	bal	–	–	0.0027	0.001	<0.0001	0.001	0.0007	–		
Zn	–	bal	–	–	–	0.015	–	0.012	0.003		
Al	–	0.01	bal	–	–	0.03	–	–	0.03	0.01	0.01

Fig. 4 Schematic representation of samples extracted along the length of the casting for further microstructural characterization

The segregation analyses were carried out in a fluorescence spectrometer (FRX), model Rigaku RIX 3100 to estimate local average concentration through an area of 100 mm^2 probe. Thermal analysis was performed using a differential scanning calorimeter (DSC) Netzsch, model 200 F3 Maia.

The size and distribution of Bi particles in the microstructure of the ternary alloys, as well as the secondary dendrite arm spacings and eutectic spacings (lamellar and fibrous), were analyzed in transverse samples of the DS castings using the image processing software ImageJ. Schematic measurements are shown in Fig. 5. For the measurements of particles diameters and distribution, the micrographs taken for each position were binarized and treated in order to permit the amount and size of the particles in the image to be calculated, as shown in Fig. 5a. The secondary dendritic arm spacing (λ_2) was obtained by the intercept method [24], based on the average distance between the center of three adjacent secondary arms (Fig. 5b). The measurement of the eutectic lamellar spacing was obtained by averaging the distance between lamellae, according to the scheme of Fig. 5c. The triangle method [24, 25] was used for direct measurements of the eutectic fiber spacing (Fig. 5d).

Results and discussion

Thermal and calorimetric analyses

Figure 6 shows the experimental cooling curves for the eight thermocouples positioned inside the DS alloys castings. For thermocouples closer to the cooled bottom of the castings, a sharper drop in temperature can be observed, while for the other thermocouples the rate of cooling decreases progressively accompanying the increase in the thermal resistance associated with the increasingly thickness of the solid layer from the heat-extracting base. In addition, it is noted that before the onset of solidification (time = 0 s), there is already a thermal gradient in the liquid metal provided by the solidification device, and for this reason, the thermocouple that is positioned closest to the cooled bottom of the casting was taken as the starting reference temperature of the experiment.

Figure 7a, b illustrates the evolution of the time of passage (*t*) of the liquidus isotherms and of the eutectic/monotectic fronts, respectively, by each thermocouple position (*P*) along the length of the Zn–8 mass% Al and ternary alloys castings. It can be noted that the proposed power functions ($P = at^b$), which were fitted to the experimental points, are appropriate to represent the correlation between *P* and *t*. The Zn–8 mass% Al and the ternary Zn–8 mass% Al–2.3/3.0 mass% Bi alloys present similar *P* versus *t* behavior with respect to the evolution of liquidus, eutectic and monotectic isotherms. On the other hand, the Zn–8 mass%–Al–1.5 mass% Bi alloy shows a distinct behavior, characterized by a slower displacement of the isotherms. Possibly, an explanation for this fact could be the lower wettability of this alloy on the carbon steel sheet (used in the solidification setup to separate the bottom of the casting from the cooling water) as compared to those of the three other alloys.

The experimental cooling rate points were determined by computing the time-derivative (d*T*/d*t*) of each cooling curve immediately after the passage of liquidus ($\dot{T}_L$) and eutectic/monotectic isotherms ($\dot{T}_E$/$\dot{T}_M$) by each thermocouple (Fig. 8). The cooling rate profiles have been characterized by power functions of the form $\dot{T} = cP^{-d} - e$, fitted to the experimental scatter along the length of each DS casting. However, this function cannot be applied near the bottom of the DS casting (*P* = 0) and care should be exercised when applying these expressions to the beginning of solidification. The subscripts L, E and M refer to liquidus, eutectic and monotectic isotherms, respectively. The cooling rate profiles of the liquidus and eutectic/monotectic isotherms for the Zn–8 mass%–Al–1.5 mass% Bi alloy casting present a behavior that is similar to that observed in Fig. 8, that is, they are lower as compared to the profiles of the other examined alloys. It can also be noted that all the cooling rate profiles stabilize just after a position in the castings of about 30 mm. The profiles of the other three examined alloys have similar behavior; therefore, they can be represented by a single power function experimental law.

The velocities (*V*) characterizing the displacement of liquidus, eutectic and monotectic isotherms come from the experimental correlations between *P* and *t*. The derivatives of the experimental $P = at^b$ functions with respect to time (d*P*/d*t*) result in the growth rate profiles shown in Fig. 9, where two distinct curves are required to represent the analyzed alloys. That is, the growth rate profile for the Zn–8 mass%–Al–1.5 mass% Bi alloy casting is different from the others and is also the lowest one.

Fig. 5 Representative schemes of the techniques used to quantify the microstructural spacings: **a** size and distribution of Bi particles; **b** secondary dendritic arm spacing (λ_2); **c** eutectic lamellar spacing (λ_L); **d** eutectic fiber spacing (λ_F)
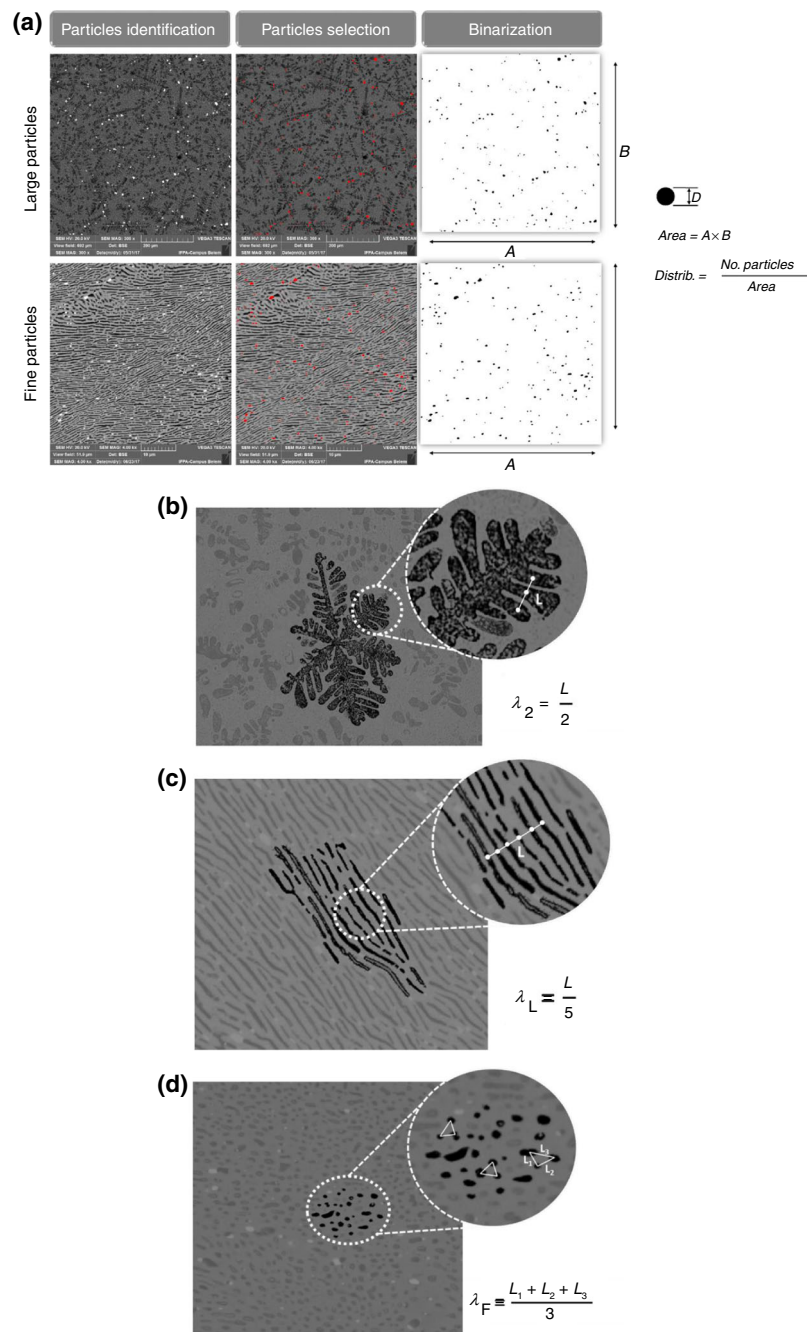
One of the difficulties to work with alloys containing elements with relatively high differences in density, as shown in Table 2, is to preview the phases distribution in the as-solidified microstructure [21, 26]. For Bi-based monotectic alloys, the homogeneous distribution of Bi, by conventional casting methods, has been a challenge due to the rapid nucleation and diffusional growth of liquid Bi droplets in the global liquid, intensified by the action of Stokes and Marangoni motion, which provides collisions and coalescence of Bi droplets followed by sedimentation induced by gravity [26, 27]. However, in the case of the alloys studied in this work (Zn–Al–Bi), it has been found that the segregation due to gravity effects probably does not occur because of the high solidification kinetics that induces short-range displacement of the Bi-rich liquid. Figure 10 shows the solute profiles along the length of the DS castings, determined by X-ray fluorescence. For all examined ternary alloys, the composition of Bi remained approximately constant and close to the nominal Bi concentration of each alloy (Fig. 10b), as well as the
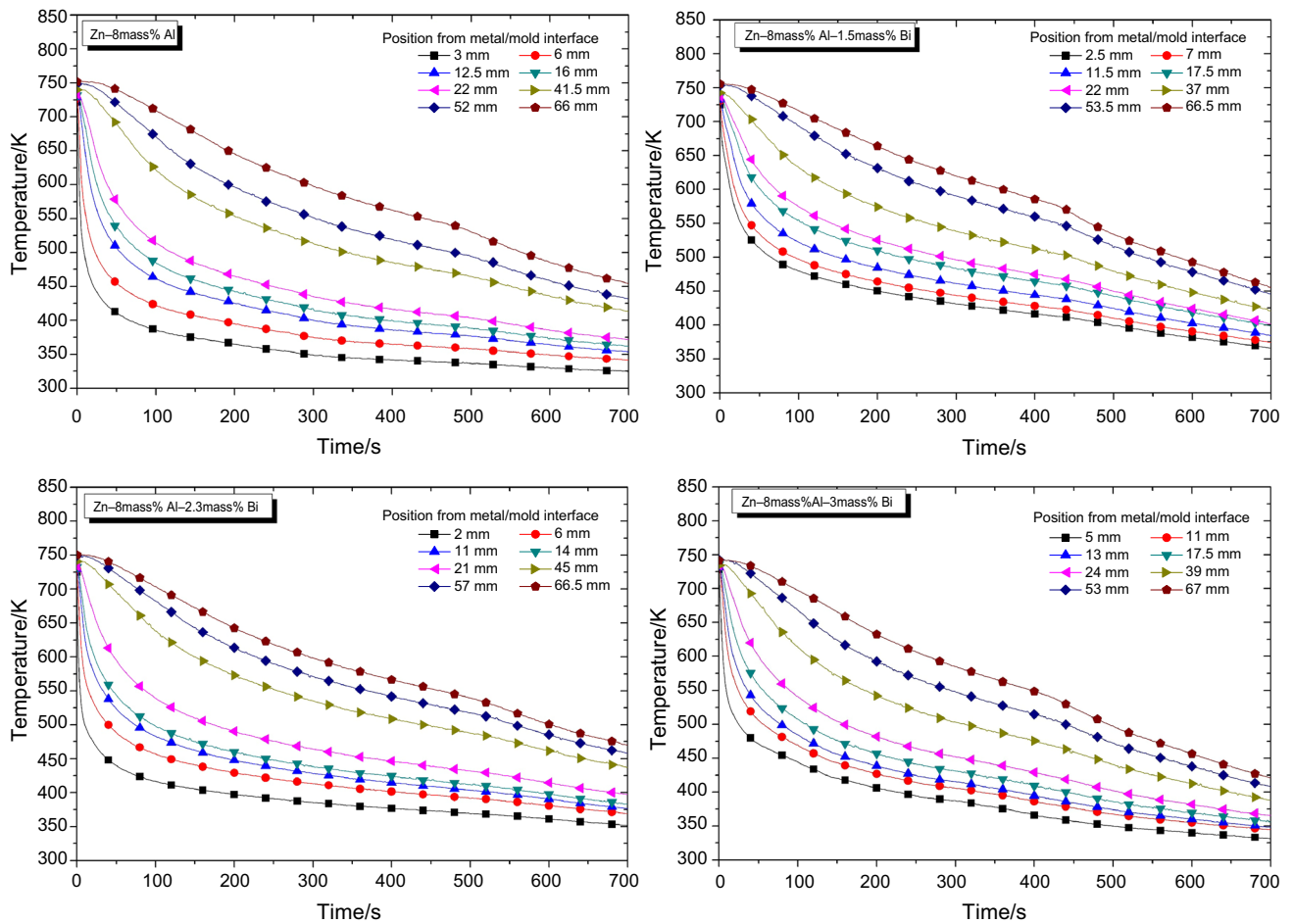
Fig. 6 Experimental cooling curves obtained by different thermocouples positioned along the length of the DS Zn–Al and Zn–Al–Bi alloys castings
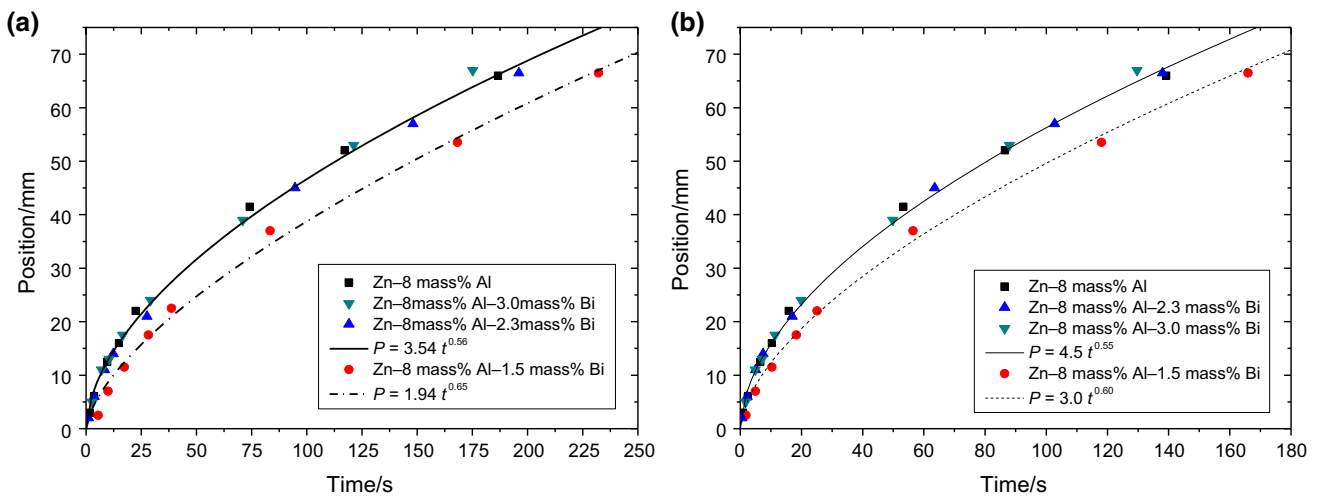

Fig. 7 Experimental displacement of characteristic isotherms along the length of the DS alloys castings: P (mm) is the thermocouple position from the cooled bottom of the casting and t (s) is time:

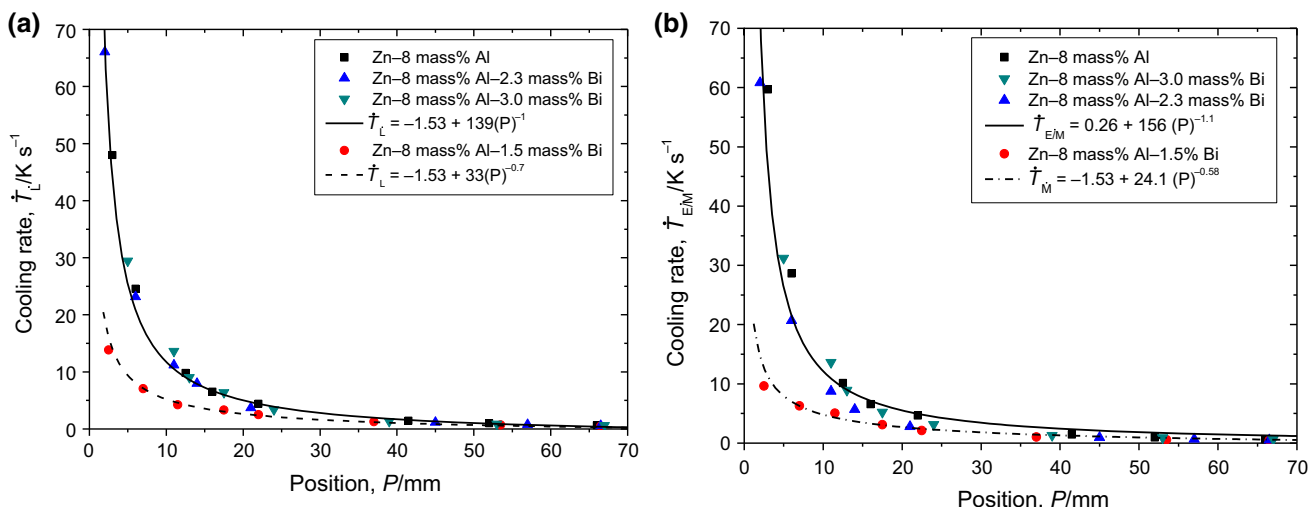**a** liquidus isotherm and **b** eutectic isotherm for the Zn–8 mass% Al alloy and monotectic isotherm for the Zn–8 mass% Al–X mass% Bi alloys

Fig. 8 Cooling rate as function of P for the Zn–8 mass% Al and Zn–8 mass% Al–X mass% Bi alloys castings: **a** liquidus isotherm ($\dot{T}_L$), and **b** eutectic isotherm ($\dot{T}_E$) for the Zn–8 mass% Al alloy and monotectic isotherm ($\dot{T}_M$) for the Zn–8 mass% Al–X mass% Bi alloys
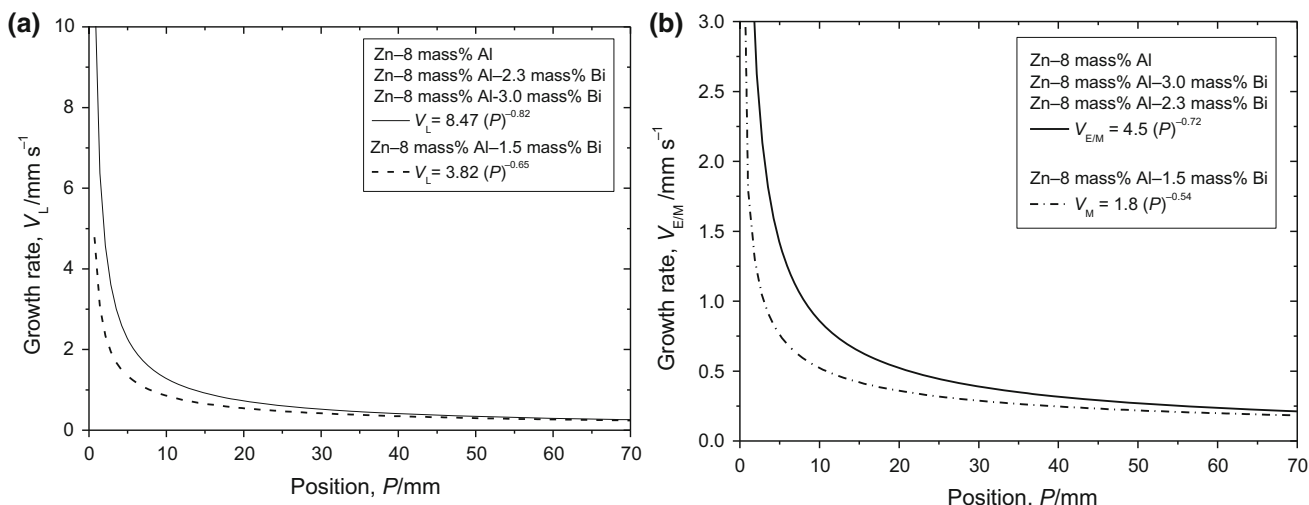

Fig. 9 Velocity profiles characterizing the displacement of representative solidification isotherms: **a** liquidus isotherm (V_L) and **b** eutectic isotherm (V_E) for the Zn–8 mass% Al alloy casting and monotectic isotherm (V_M) for the Zn–8 mass% Al–X mass% Bi alloys castings

Table 2 Density/kg m^{-3} of metals composing the examined alloys [28]

Zn	Al	Bi
7100	2699	9800

concentration of Al that remained in the range 7.5–8.0 mass% Al (Fig. 10a), which does not configure the occurrence of macrosegregation.

In order to confirm the temperatures of each invariant reaction that occurs along cooling from the melt of each examined alloy, additional analyses using differential scanning calorimetry (DSC) have been performed. Figure 11 shows the experimental DSC curves for the Zn–8 mass% Al and Zn–8 mass% Al–X mass% Bi (X=1.5; 2.3; and 3.0) alloys. The cooling rate used in the DSC tests was

0.0083 °C s^{-1}. The endothermic curve of Fig. 11a (binary alloy) shows that at 683 K occurs the formation of the first solid phase originated through the reaction L↔L′+(Al′), with the primary dendrites being constituted by a Zn-rich solid solution and the face-centered cubic metastable phase (Al′) by proeutectic dendrites.

Following the solidification path of the binary alloy, the remaining liquid continues to be enriched by solute until the eutectic concentration is reached. At 654 K (eutectic temperature), all remaining liquid solidifies as a eutectic mixture formed by eutectic (Zn) and eutectic (Al′) phases, through the reaction L↔(Al′)+(Zn) where the (Zn) phase is a Zn-rich phase with a hexagonal close packed (hcp) crystal structure and the (Al′) phase is also a Zn-rich phase, well reported in the literature as (α′) [29], with a face-
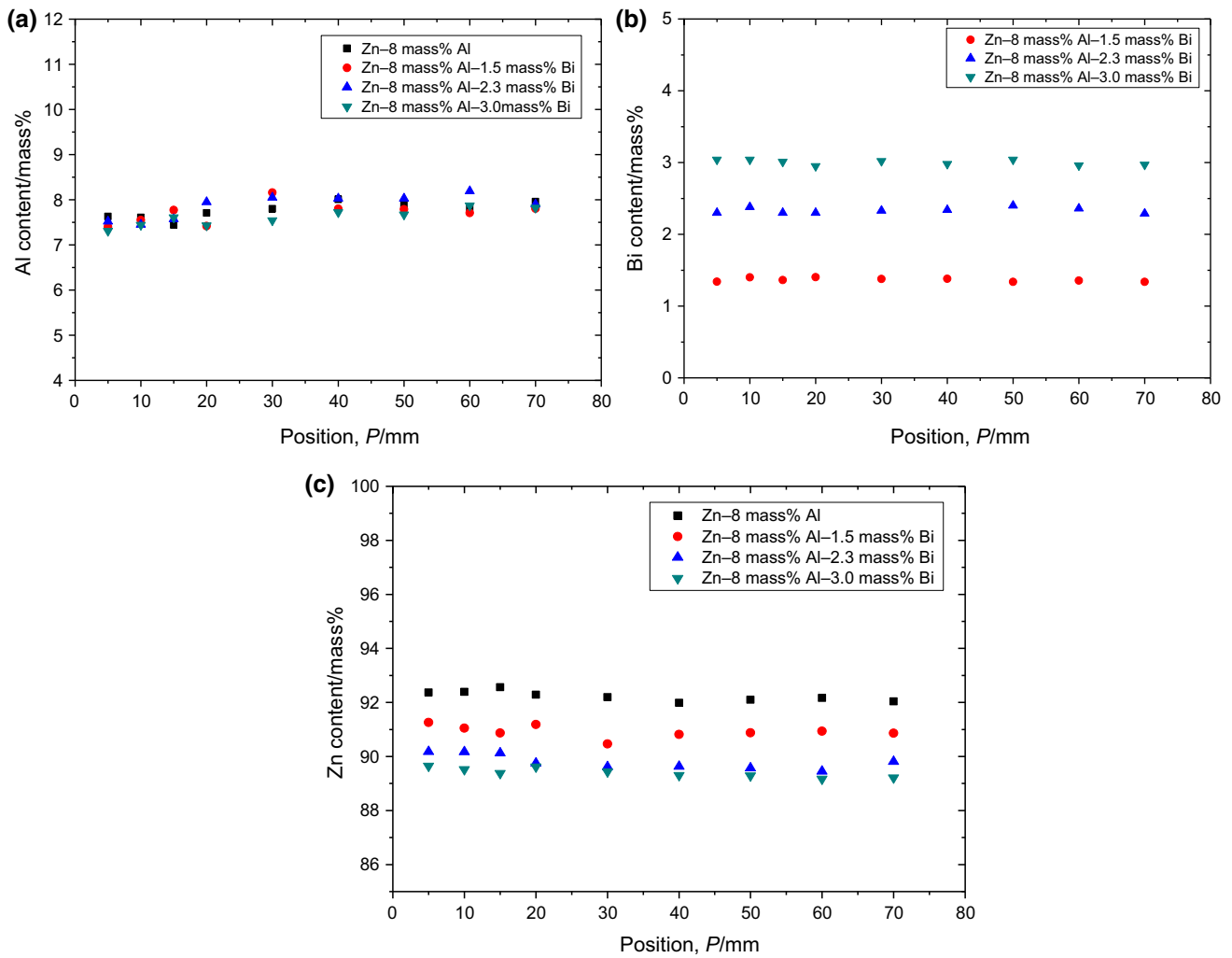
Fig. 10 Experimental Al, Bi and Zn concentration profiles along the length of the DS Zn–Al and Zn–Al–Bi alloys castings
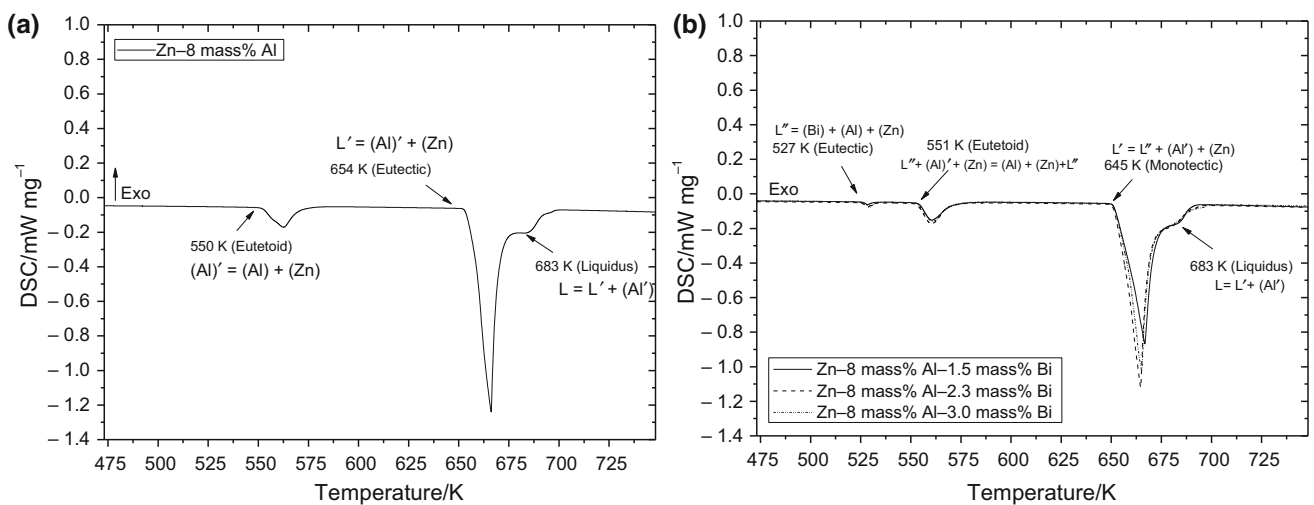

Fig. 11 Differential scanning calorimetry of **a** Zn–8 mass% Al alloy and **b** Zn–8 mass% Al–X mass% Bi (X=1.5; 2.3 and 3.0 mass%) alloys at a cooling rate of 0.083 °C s^{-1}
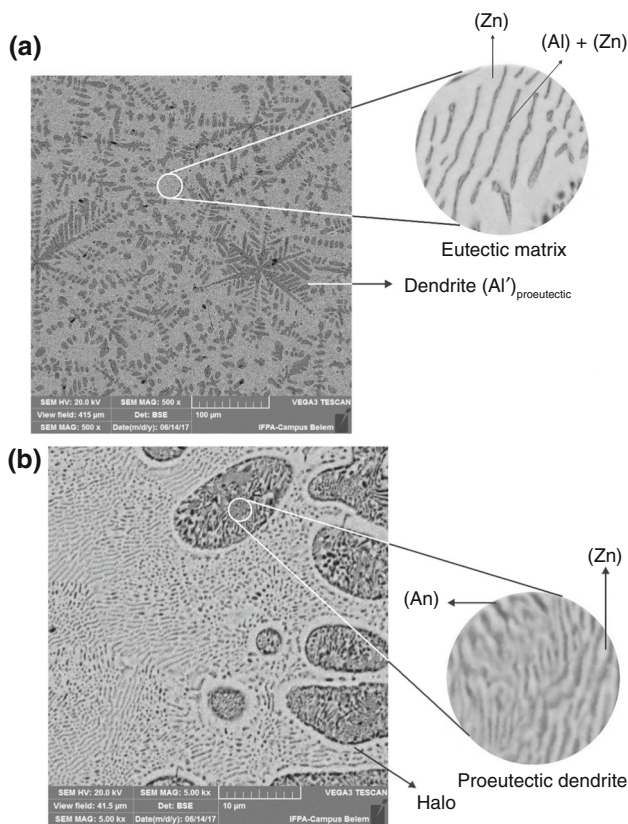
(a)

(b)

Fig. 12 Typical microstructure of the Zn–8% Al alloy highlighting **a** eutectic matrix, **b** proeutectic dendrite

centered cubic (fcc) crystal structure. At 550 K, it can be observed that the (Al′) phase becomes unstable, and hence, it undergoes a eutectoid transformation: (Al′)↔(Al)+

(Zn). These reactions agree with those shown in the phase diagram of Fig. 2. It is worth noting that both the proeutectic (Al′) phase and the (Al´) phase from the eutectic mixture are expected to undergo the eutectoid transformation.

Figure 11b shows the curves resulting from the DSC tests for the three examined ternary alloys. At 410° C, the first dendrites arise from the reaction L↔ L′+(Al′). The analysis was not sensitive enough to accurately determine the liquidus temperature of each alloy, so only the temperature of 683 K is indicated in the figure. The remaining liquid undergoes a monotectic four-phase reaction L′↔L″+(Al′)+(Zn) at 645 K, where L′ is an Al-rich liquid and L″ is a Bi-rich liquid [30]. The (Al′) phase decomposes through the eutectoid four-phase reaction (Al)′+(Zn)+L″↔(Al)+(Zn)+L″ at 551 K, into (Al) and (Zn) phases [29, 31].

The last invariant reaction of the Zn–Al–Bi system refers to the eutectic reaction: (L″)↔(Al)+(Zn)+(Bi). The Bi-rich liquid L″ solidifies at 527 K, forming the Bi droplets. All these reactions in the ternary alloys, as determined by the DSC tests, are also in agreement with those shown in the phase diagram of Fig. 3. It is worth mentioning that the microstructural arrangement, except for changes due to the solid-state transformations, is practically defined after the monotectic reaction. The last liquid (L″) to solidify, which is practically pure bismuth, is already with its determined configuration in the solid matrix established after the monotectic reaction.
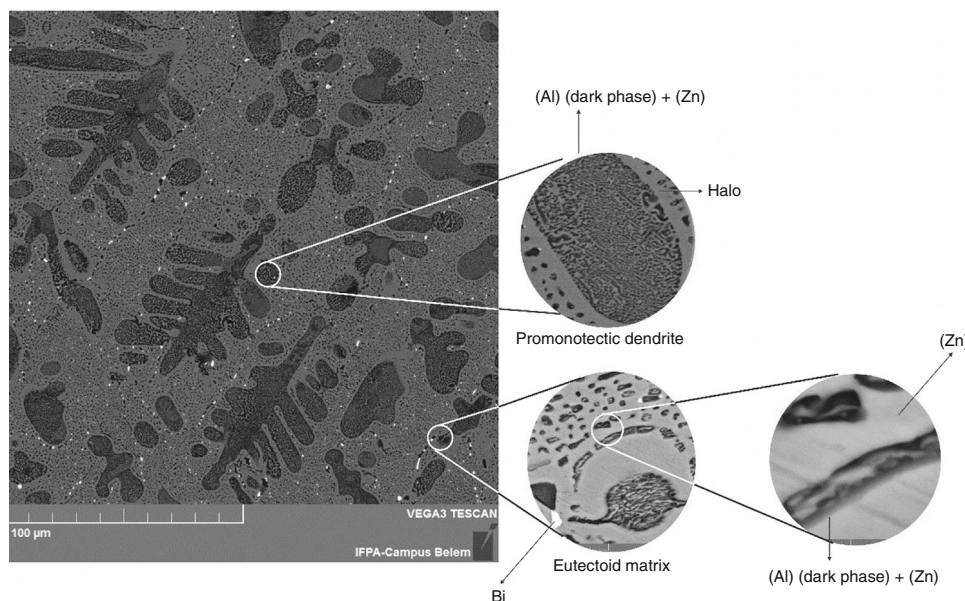

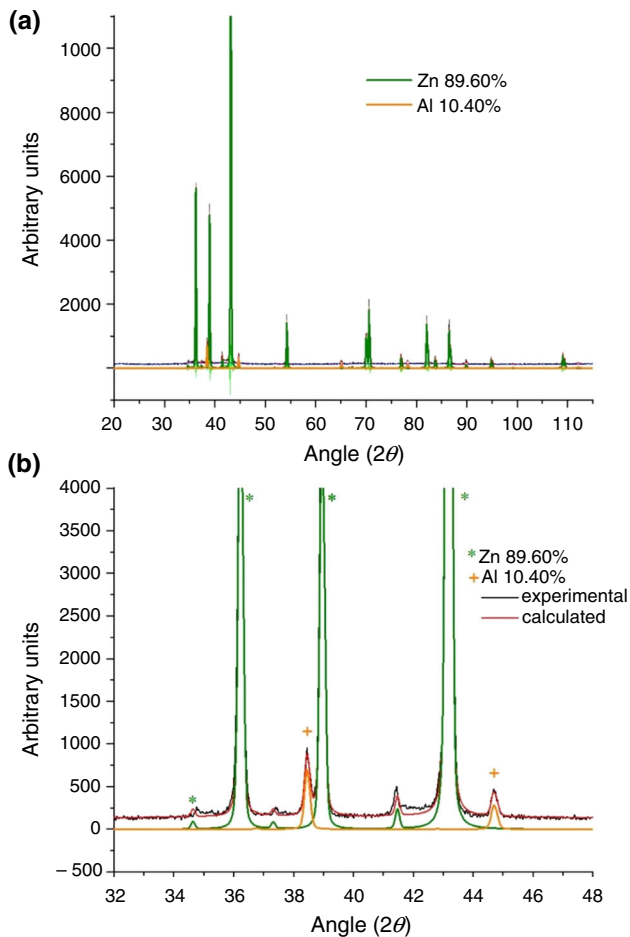**Fig. 13** Typical microstructure of Zn–8 mass% Al–X mass% Bi hypomonotectic alloys

(a)

(b)

Fig. 14 Diffractograms obtained by XRD analysis and by the Rietveld method for a Zn–8 mass% Al alloy sample: **a** general diffraction, **b** extended diffractogram

(a)

(b)

Fig. 15 Diffractograms obtained by XRD analysis and by the Rietveld method for a Zn–8 mass% Al–2.3 mass% Bi alloy sample: **a** general diffraction, **b** extended diffractogram

Microstructural characterization: optical microscopy (OM), scanning electron microscopy (SEM) and X-ray diffraction (XRD)

Figure 12 shows the typical microstructure of the unidirectionally solidified Zn–8 mass% Al alloy. As can be observed, the resulting microstructure is formed by the product of the eutectoid transformation [(Al′)↔(Al)+(Zn)], both within the eutectic mixture (Fig. 12a) and in the dendritic proeutectic (Al′) phase, resulting in alternate lamellae of (Al) and (Zn) (Fig. 12b).

Compared to the binary alloy, the ternary alloys actually have quite similar invariant reactions. While the binary alloy is mainly characterized by a eutectic reaction, the ternary alloys have also a monotectic reaction. Although the presence of Bi in the ternary alloys causes changes in the set of invariant reactions and in the temperature at which they occur, practically it acts only as an immiscible element within the Zn–Al binary system, and in general microstructural terms the difference is the additional
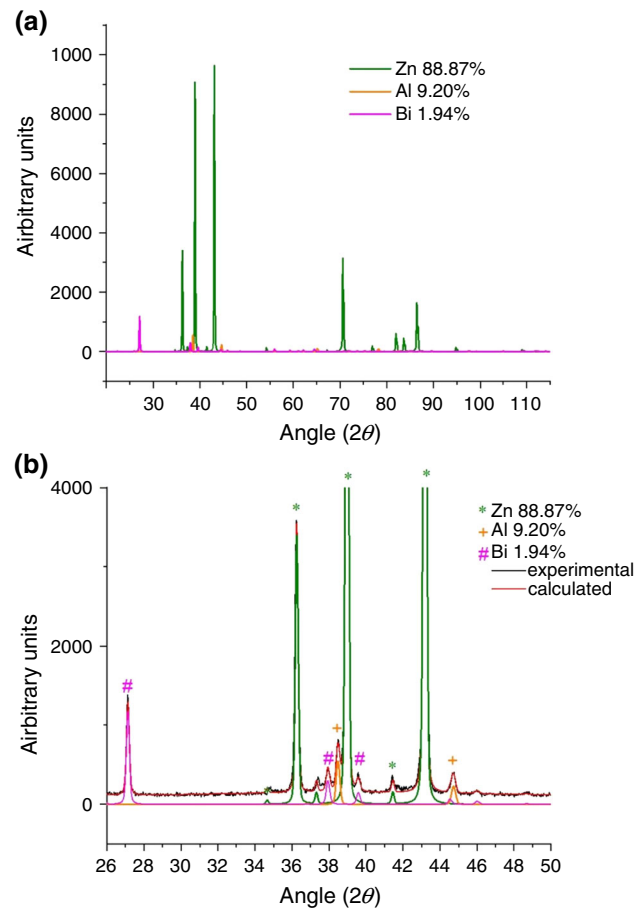
presence of Bi in a typical microstructure of a Zn–8 mass% Al binary alloy, as can be seen in Fig. 13.

Figure 13 also shows a halo of (Zn) around the promonotectic dendrite, as also reported in the literature [32, 33]. Yang et al. [33] reported that the halo only occurs in Zn–Al hypereutectic alloys for Al>5 mass%, without any possibility of occurring for eutectic and hypoeutectic alloys (Al<5%). Another influence factor analyzed by Yang et al. is related to the thickness of the halo in a Zn–6.3% Al alloy. They have also observed that the higher the cooling rate, the lower the halo thickness. In binary alloy systems, the formation of halos is dependent on the supercooling required for nucleation of the primary and eutectic phases. According to theory [32], the halo thickness should be proportional to the supercooling required for the nucleation of the secondary phase, and the halo will only exist when the primary phase is not a good secondary phase nucleating agent. For the particular cases of the studied Zn–Al and Zn–Al–Bi alloys, a higher supercooling is required by the (Al) phase to grow on (Zn) than that required by (Zn) to grow on the (Al) phase.
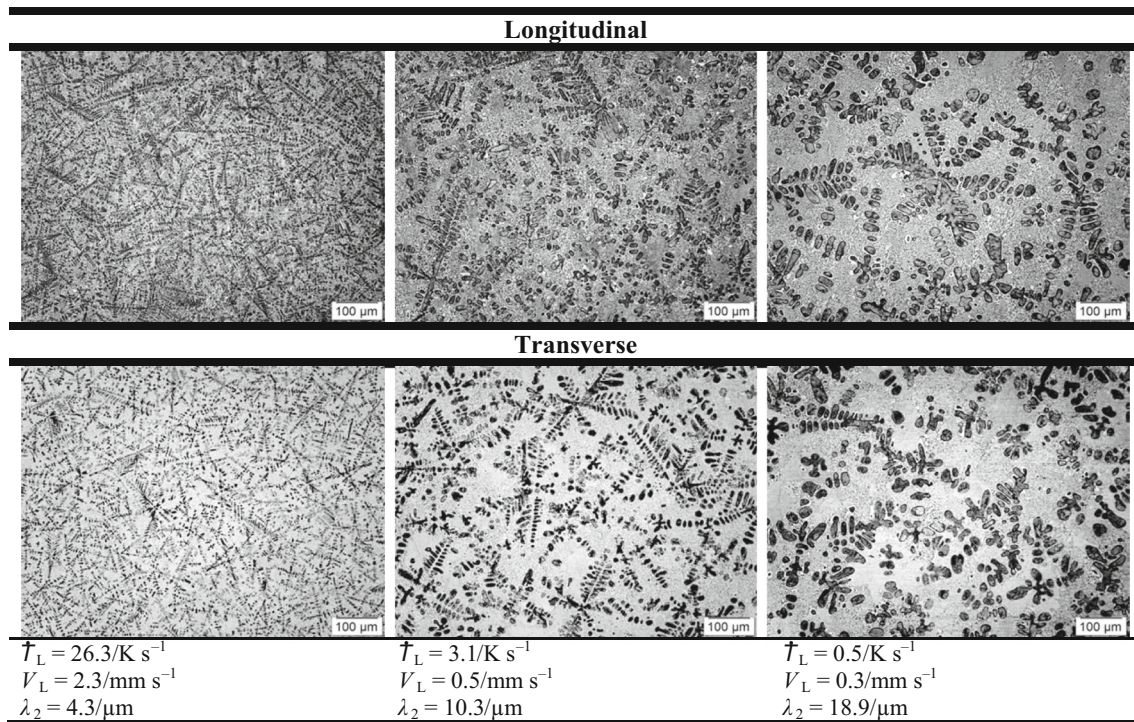
Longitudinal

Transverse

$\dot{T}_L = 26.3/\text{K s}^{-1}$ $\dot{T}_L = 3.1/\text{K s}^{-1}$ $\dot{T}_L = 0.5/\text{K s}^{-1}$
$V_L = 2.3/\text{mm s}^{-1}$ $V_L = 0.5/\text{mm s}^{-1}$ $V_L = 0.3/\text{mm s}^{-1}$
$\lambda_2 = 4.3/\mu\text{m}$ $\lambda_2 = 10.3/\mu\text{m}$ $\lambda_2 = 18.9/\mu\text{m}$

Fig. 16 Typical microstructures along the length of the DS Zn–8 mass% Al alloy casting

Longitudinal

Transverse

$\dot{T}_L = 26.3/\text{K s}^{-1}$ $\dot{T}_L = 3.1/\text{K s}^{-1}$ $\dot{T}_L = 0.5/\text{K s}^{-1}$
$V_L = 2.7/\text{mm s}^{-1}$ $V_L = 0.5/\text{mm s}^{-1}$ $V_L = 0.3/\text{mm s}^{-1}$
$\lambda_2 = 5.0/\mu\text{m}$ $\lambda_2 = 12.0/\mu\text{m}$ $\lambda_2 = 19.0/\mu\text{m}$
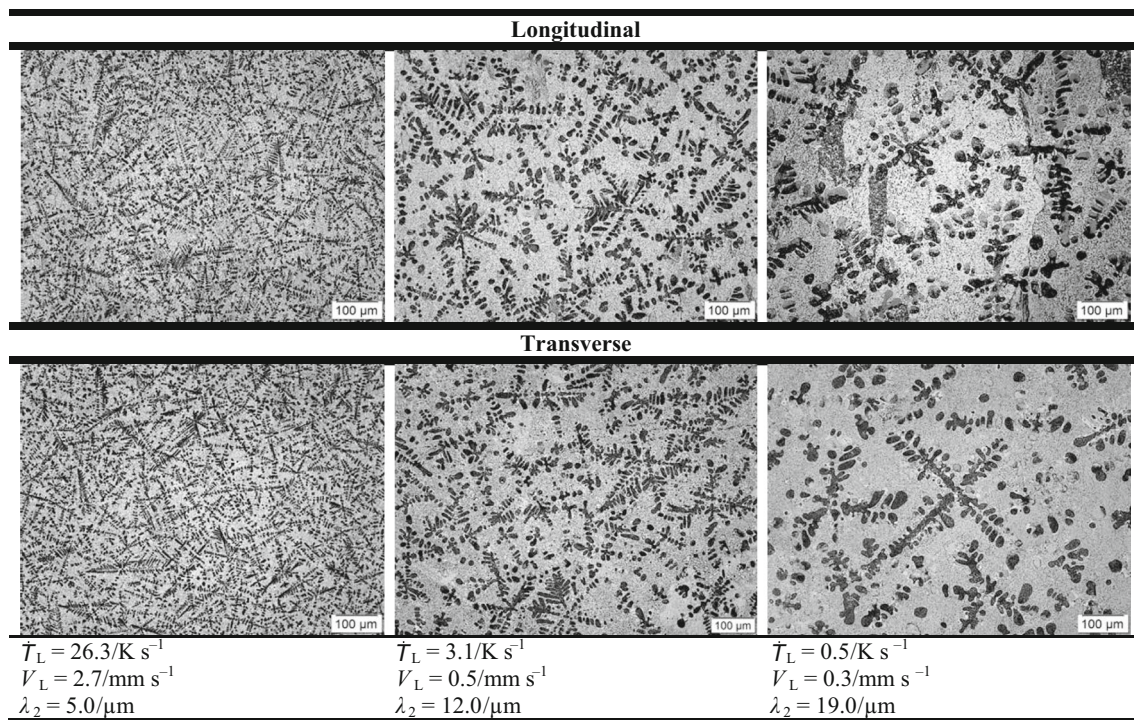
Fig. 17 Typical microstructures along the length of the DS Zn–8 mass% Al–3.0 mass% Bi alloy casting

The diffractograms obtained by the X-ray diffraction (XRD) analyses of Zn–8 mass% Al and Zn–8 mass% Al–2.3 mass% Bi alloys samples from the position 20 mm in the DS castings are shown in Figs. 14 and 15, respectively.

This ternary alloy was chosen as representative since what differs the ternary alloys is only the Bi content. (Al), (Zn) and (Bi) were identified, confirming the phases predicted by the phase diagram of Fig. 3. The Rietveld method was
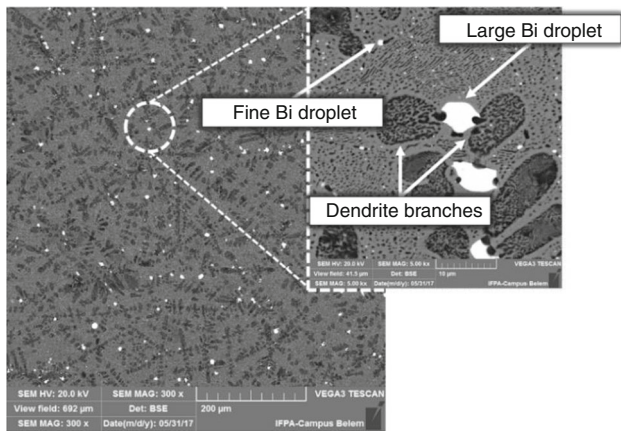
Fig. 18 SEM/BSE micrograph of a Zn–8 mass% Al–3.0 mass% Bi alloy sample

applied to quantify the detected phases. The Zn–8 mass% Al alloy sample was quantified as having 89.6% of the (Zn) phase and 10.4% of the (Al) phase. The crystalline lattice parameters of the (Zn) phase were $a=2.665337$ Å and $c=4.950860$ Å, while that of the (Al) phase, $a=4.04833$ Å.

For the Zn–8 mass% Al–2.3 mass% Bi alloy, the sample was quantified as having 88.87% of (Zn), 9.2% of (Al) and 1.93% of (Bi). The crystalline lattice parameters of the (Zn) phase were $a=2.666648$ Å and $c=4.944966$ Å, while for the (Al) phase, $a=4.04831$ Å and finally (Bi) with $a=4.54684$ Å and $c=11.8641$ Å. Through these results, it can be affirmed that there was a complete transformation of the (Al′) phase into (Al) and (Zn); therefore, no evidence of the metastable phase (Al′) at room temperature was detected.

The optical micrographs in Figs. 16 and 17 show the typical microstructures of Zn–8 mass% Al and Zn–8 mass% Al–3 mass% Bi alloys castings, respectively, with images of transverse and longitudinal sections. Three positions were chosen to illustrate the evolution of the microstructures for: high, medium and low solidification cooling rates. These values of cooling rates, as well as those of growth rate and secondary dendritic arm spacing are also shown in each figure. For higher cooling rates, the microstructure is more refined. As the rate decreases, the microstructure becomes coarser.
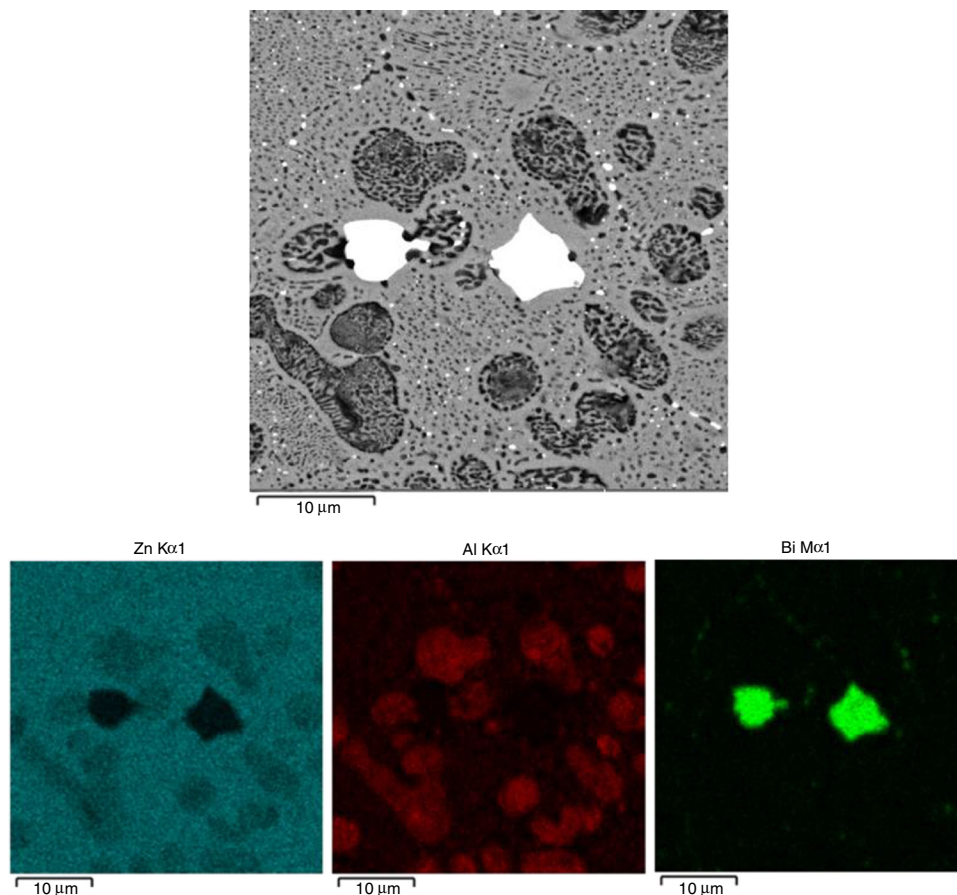

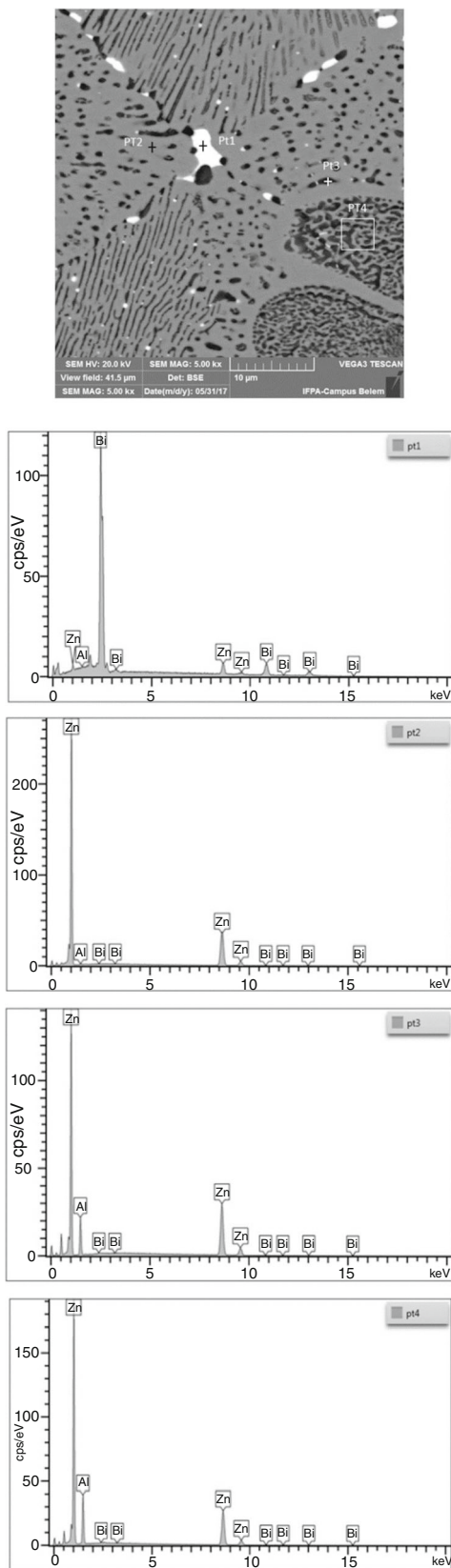**Fig. 19** Map-scan of a Zn–8 mass% Al–3.0 mass% Bi alloy sample from P 05 mm in the DS casting

Fig. 20 EDS analyses of a Zn–8 mass% Al–3.0 mass% Bi alloy sample from P 70 mm in the DS casting

Table 3 EDS analyses of a Zn–8 mass% Al–3.0 mass% Bi alloy sample from P 70 mm in the DS casting

Point	Element/mass%		
	Zn	Al	Bi
Pt1	10.77	0.09	89.15
Pt2	99.22	0.65	0.13
Pt3	86.00	13.48	0.52
Pt4	77.56	22.00	0.43

The difference between the microstructures of the binary and the ternary alloys is basically characterized by the presence of Bi in the ternary alloys. As the micrographs in Figs. 16 and 17 are images acquired by OM, Bi is not evidenced. The best technique to observe Bi in micrographs is that provided by SEM in backscattered electrons mode (BSE), where the phase with the element of superior atomic mass (Bi) appears brighter in the images, as shown in Fig. 18.

It is worth noting that the microstructure of the ternary alloys is characterized by the presence of two types of Bi droplets: large particles and fine particles, generated on different moments of the solidification process. The larger droplets are product of nucleation, diffusion, collision and coalescence of the first liquid separation, which precipitates just after the formation of the first solid phase (Al′-dendrites). This is the reason for the larger droplets being located between the dendritic branches. Moreover, the fine particles are formed and trapped by the monotectic isotherm; therefore, the small droplets are disseminated into the matrix between the lamellae and fibers.

Several studies have been devoted to show that high cooling rates during the solidification process promote sensible changes in the dynamics of phases formation predicted by the equilibrium phase diagram, which may induce the precipitation of unexpected phases for a given composition, or even suppressing the formation of phases predicted for equilibrium conditions. For the investigated ternary Zn–8 mass% Al–XBi (X=1.5, 2.3 and 3 mass%) alloys, as shown by the pseudo-binary equilibrium diagram of Fig. 3, a Zn solid solution was expected to be formed in a narrow range of temperatures over 645 K, which would precipitate from the global liquid (L′). However, the microstructural characterization of the alloys by OM and SEM techniques did not reveal the occurrence of this phase, which seems to indicate that under transient conditions of heat extraction occurs the "flattening" of the phase formation field, thus suppressing the Zn-promonotectic phase. On the other hand, it is remarkable in the micrographs of the ternary alloys having 2.3 and 3 mass% Bi that, besides the fine Bi particles trapped between the lamellae generated in the monotectic transformation, large globules of Bi anchored between the dendritic arms of the (Al′) phase can be found, fact not observed for the alloy
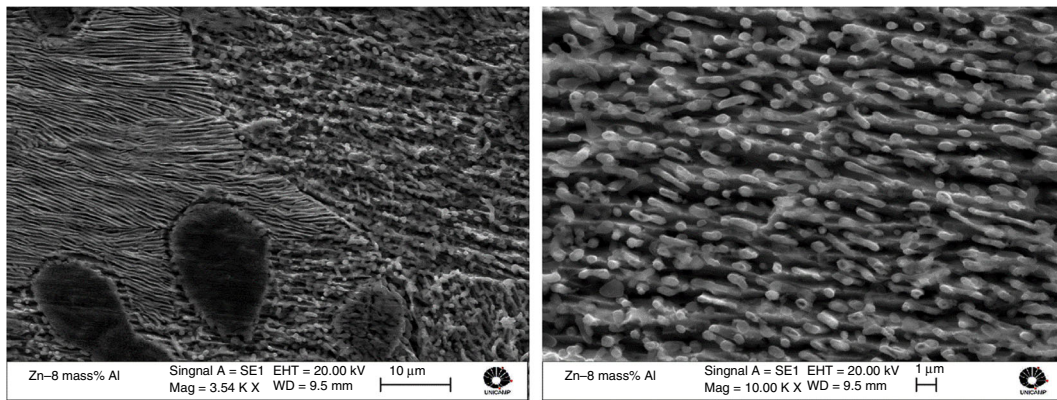
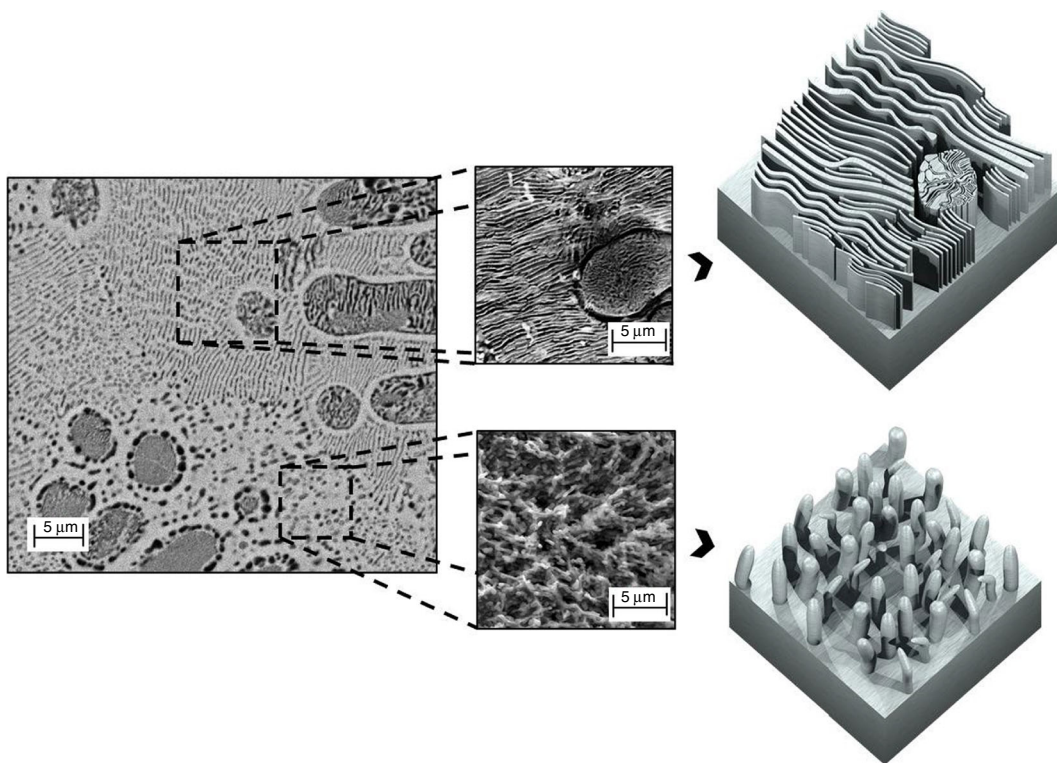**Fig. 21** Binary alloy: deep etched microstructure

Fig. 22 Scheme of the different morphologies of phases revealed in the microstructure of the binary alloy

containing 1.5 mass% Bi. It seems that the solidification far from equilibrium conditions alters the transformation line that defines the immiscibility gap of the ternary alloys by shifting, to the left, the monotectic invariant point (provided in the equilibrium phase diagram at 5.5 mass% Bi), that is, even for alloys having lower Bi concentrations (such as 2.3 and 3% Bi), the separation of liquids takes

place at temperatures above the monotectic, therefore during the growth of the (Al′) phase.

Figure 19 shows the elemental SEM–EDS mapping obtained along a transverse sample from the position 05 mm of the DS Zn–8 mass% Al–3.0 mass% Bi alloy casting. It can be observed that the ternary monotectic alloy comprises a mixture of Al and Zn in solid solution ((Al)
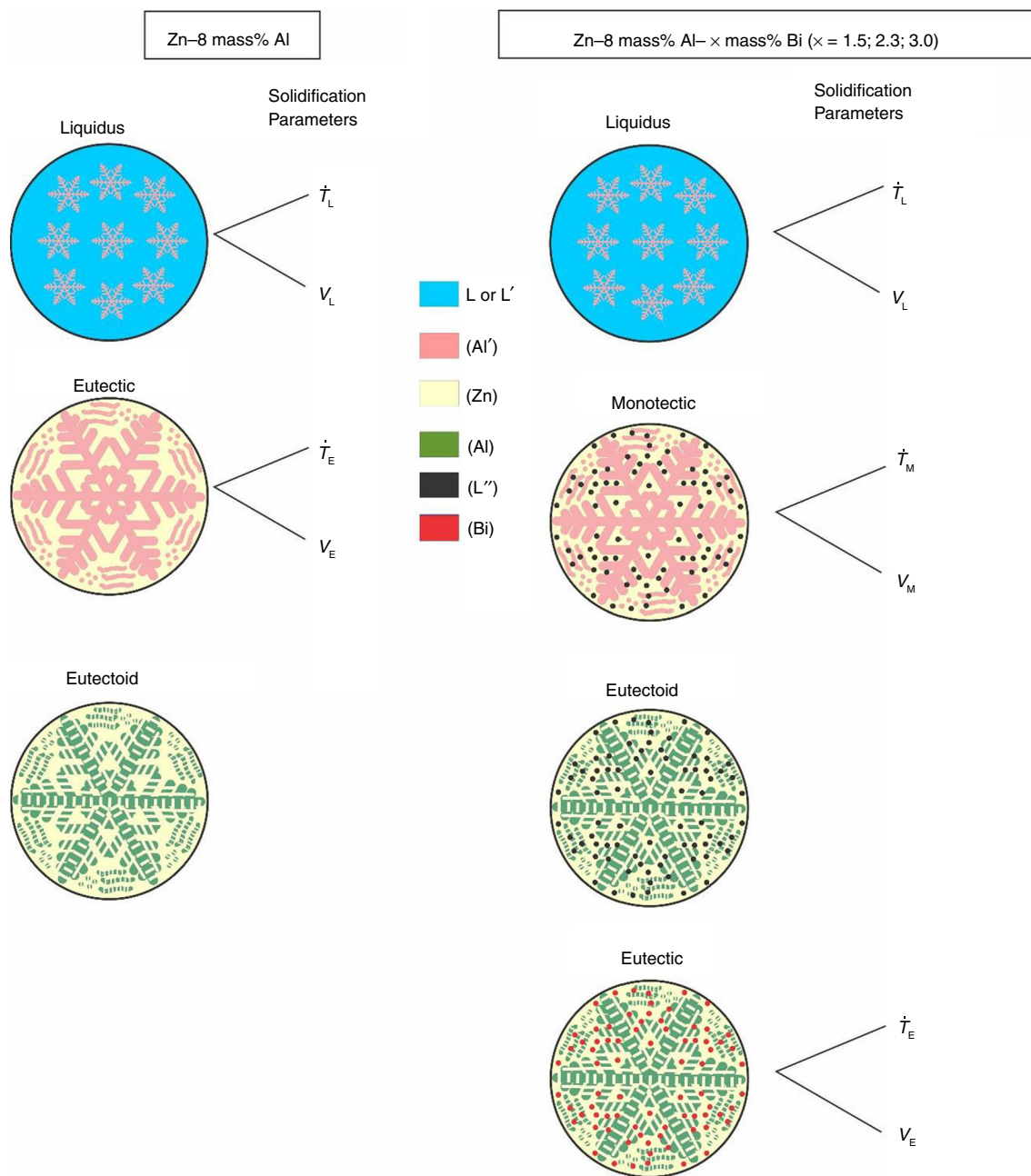
Fig. 23 Schematic evolution of microstructures of Zn–8 mass% Al and Zn–8 mass% Al–*X* mass% Bi (*X*=1.5; 2.3; 3.0) alloys—invariant reactions and solidification thermal parameters

phase and (Zn) phase). The solubility of Bi in Al and Zn is negligible; therefore, it solidifies as pure Bi droplets, as confirmed by EDS analyses in Fig. 20 and Table 3.

The primary phase developed in the form of predominantly equiaxed dendrites for both binary and ternary alloys. These dendrites are immersed in a matrix consisting of eutectoid fibers or lamellae, highlighting that these dendrites also underwent eutectoid transformation. Figure 21 shows the micrograph of a sample of the Zn–8 mass% Al binary alloy revealed by deep etching with a chemical reagent

containing 20 mass% HCl. The etching promoted the dissolution of the Zn-rich areas, confirming the presence of both lamellae and fibers in the matrix. Figure 22 presents schematically the different revealed morphologies.

Microstructural growth and correlation with solidification thermal parameters

The microstructural spacings (secondary dendritic arm spacing, λ_2, spacing between lamellae, λ_L, and fiber
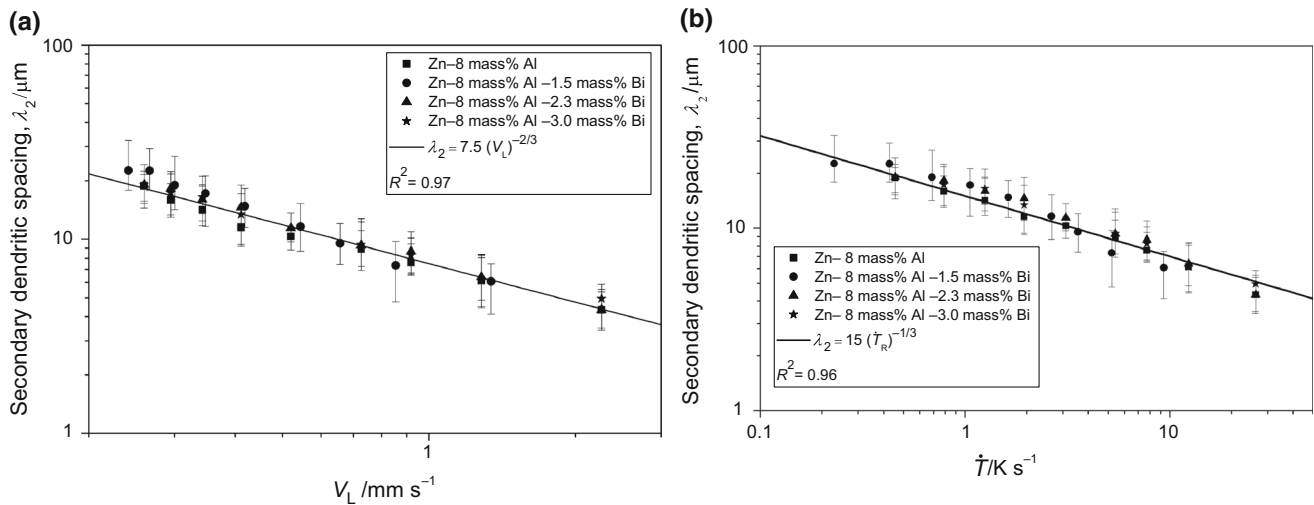
Fig. 24 Secondary dendritic arm spacing as a function of solidification thermal parameters: **a** growth rate and **b** cooling rate
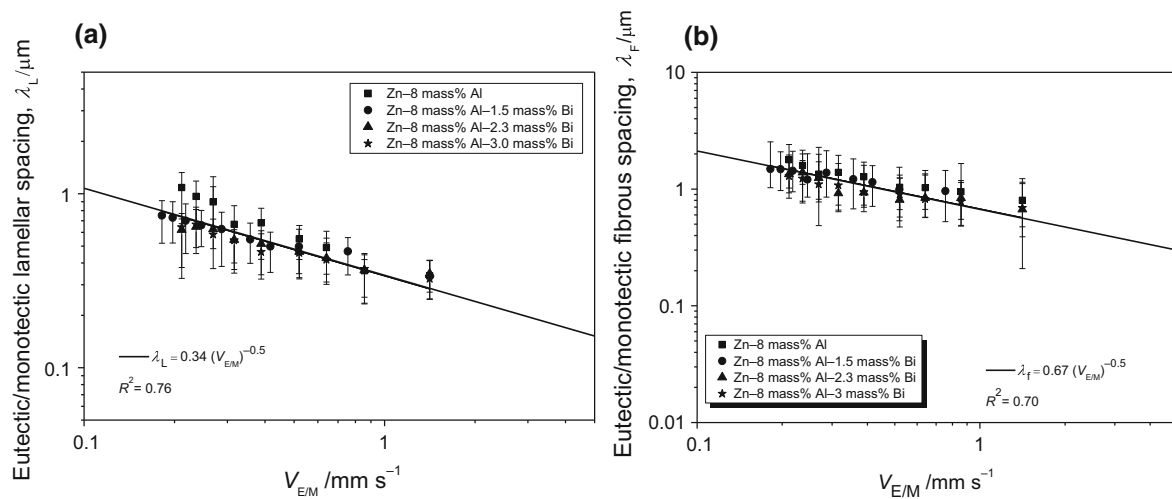

Fig. 25 **a** Eutectic/monotectic lamellar spacing (λ_L) and **b** eutectic/monotectic fibrous spacing (λ_F) as a function of the rate of displacement of the eutectic/monotectic isotherms ($V_{E/M}$)

spacing, λ_F) were measured along the length of the DS castings, according to the procedure shown in Fig. 5. The dendrites, lamellae and fibers evolve from a refined structure at regions in the casting that are closer to the cooled bottom, to increasingly coarser structures toward the top of the DS casting. After these measurements, relations between the microstructural spacings and cooling and growth rates associated with each representative isotherm (liquidus, eutectic and monotectic) were established. Figure 23 shows a schematic evolution of the microstructures of the examined alloys associated with the corresponding invariant reactions during cooling from the melt.

Figure 24 shows the secondary dendritic arm spacing associated with the thermal parameters for all analyzed alloys. It can be observed that at high cooling rates and

high rates of displacement of the liquidus isotherm (growth rate), smaller spacings are formed. The proposed experimental equations adequately describe $\lambda_2 \times \dot{T}_L$ and $\lambda_2 \times V_L$ evolutions, with the same fitted equations applying to all the four examined alloys, which indicates that the addition of Bi to the Zn–8 mass% Al alloy did not change the evolution of λ_2. The derived power functions in which the exponents $-2/3$ and $-1/3$ characterize the experimental evolution of λ_2 as a function of V_L and $\dot{T}_L$ were also reported to be applicable to several binary alloys [34–36].

The dendrites, as previously discussed, are immersed in a matrix consisting of lamellae and fibers originated from a eutectic reaction in the case of the binary alloy, and from a monotectic reaction in the case of the ternary alloys (see Fig. 23). Thus, the spacings between lamellae (λ_L) and
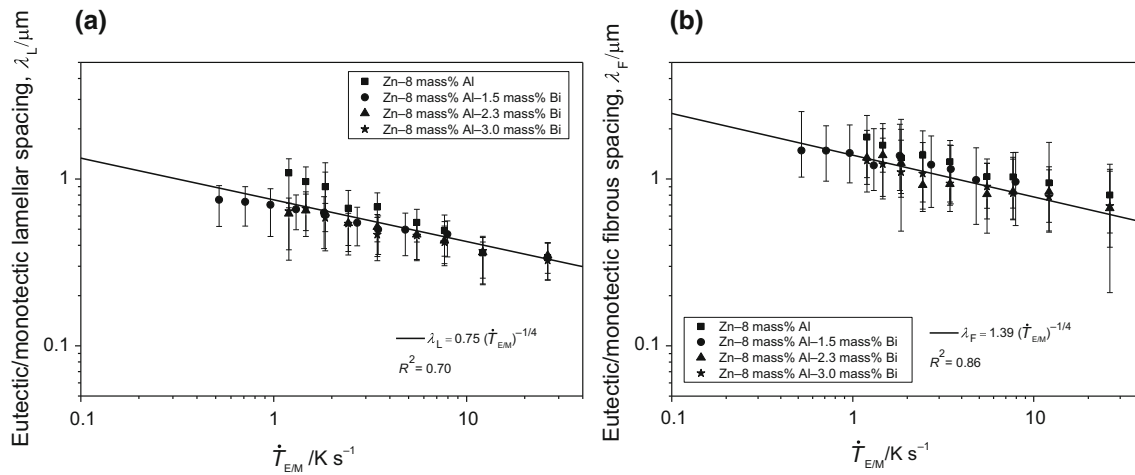
Fig. 26 **a** Eutectic/monotectic lamellar spacing (λ_L) and **b** eutectic/monotectic fibrous spacing (λ_F) as a function of the cooling rate ahead of the eutectic/monotectic isotherms ($\dot{T}_{E/M}$)
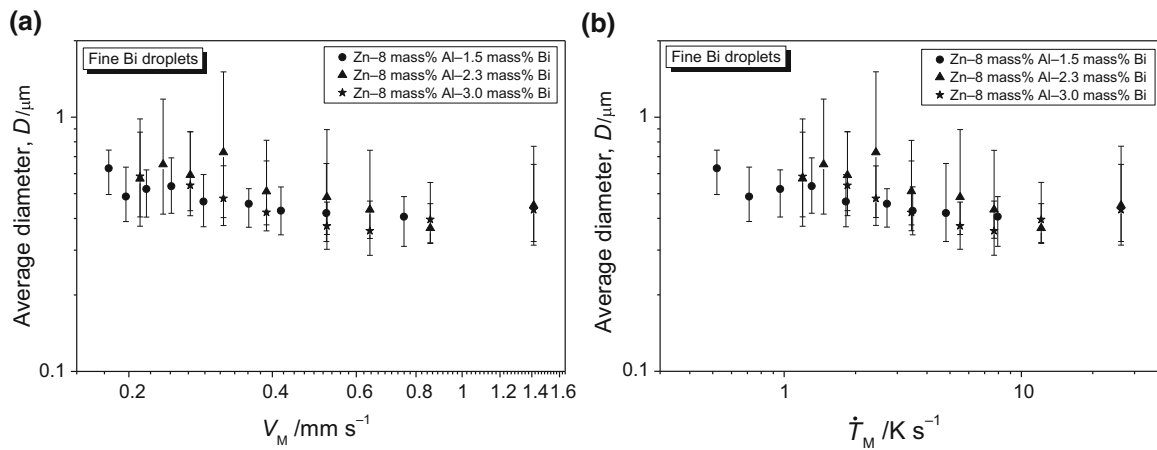

Fig. 27 Diameter of fine Bi droplets as a function of: **a** rate of displacement (V_M) and **b** cooling rate ($\dot{T}_M$) of the monotectic isotherms

Fig. 28 Area distribution of fine Bi droplets as a function of: **a** rate of displacement (V_M) and **b** cooling rate ($\dot{T}_M$) of the monotectic isotherms

(a)

(b)

Fig. 29 Diameter of larger Bi droplets as a function of: **a** rate of displacement (V_M) and **b** cooling rate ($\dot{T}_M$) of the monotectic isotherms
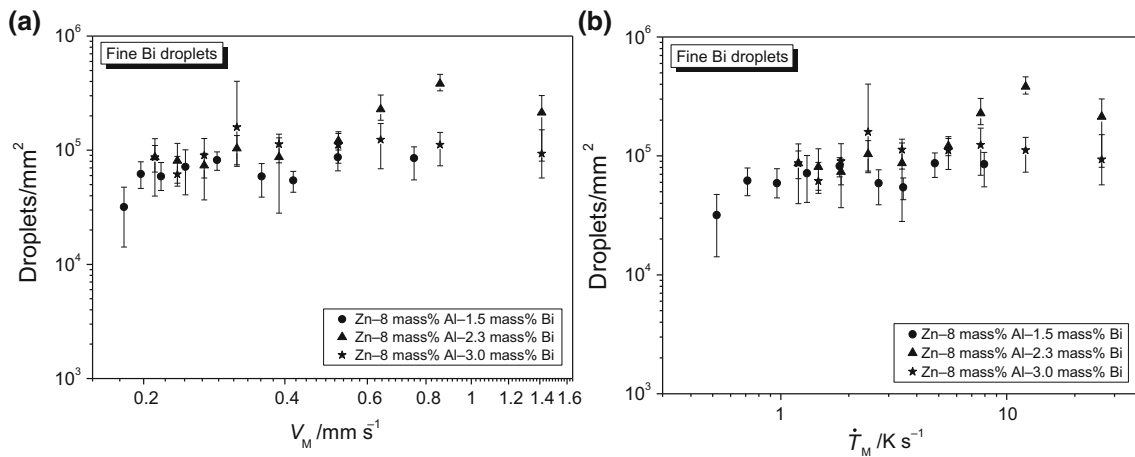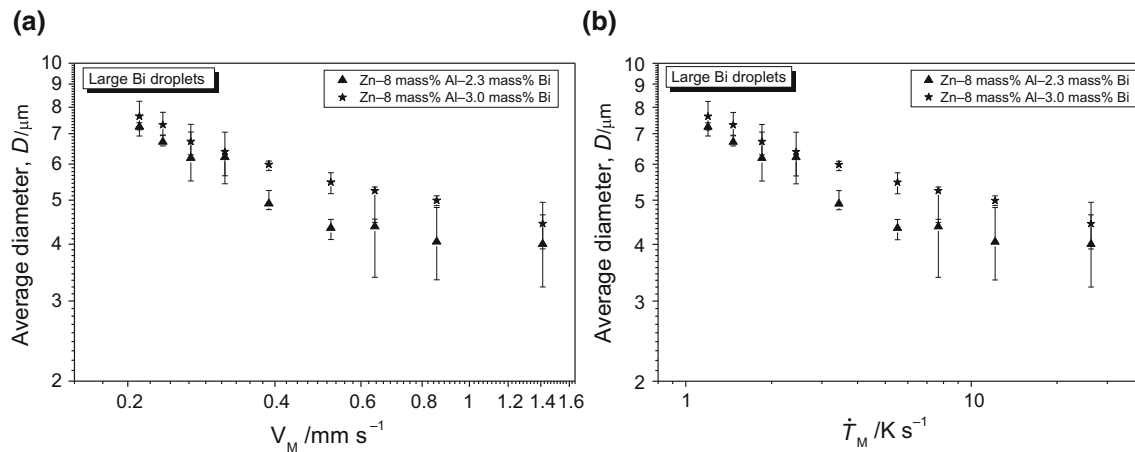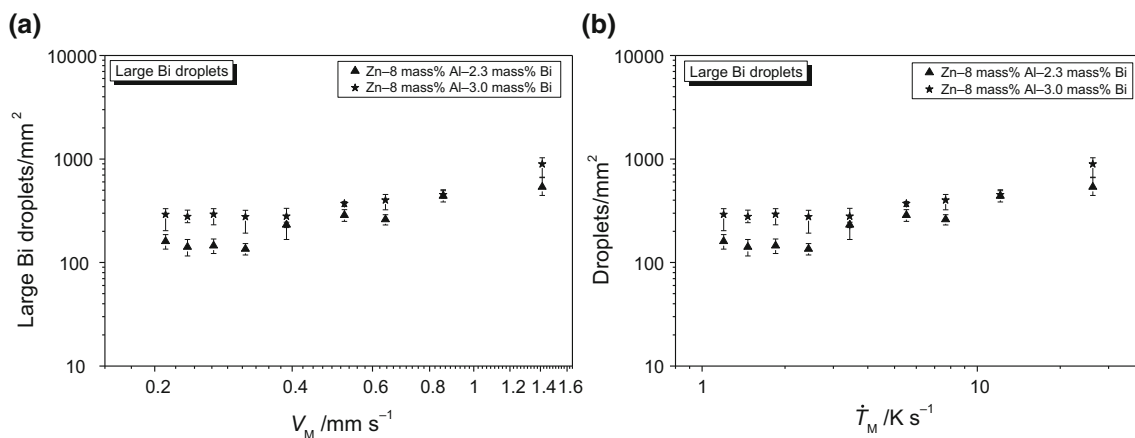
(a)

(b)

Fig. 30 Area distribution of large Bi droplets as a function of: **a** rate of displacement (V_M) and **b** cooling rate ($\dot{T}_M$) of the monotectic isotherms

between fibers (λ_F) are correlated with the rate of displacement of the eutectic isotherm (V_E) for the binary alloy and with the monotectic isotherm (V_M) for the ternary alloys (Fig. 25) and with the cooling rates ahead of these isotherms ($\dot{T}_E$ e $\dot{T}_M$) (Fig. 26). The classic Jackson and Hunt growth law for eutectics, $\lambda^2 V$=constant, seems to apply to all alloys investigated in this work. Considering that the cooling rate is given by a constant multiplied by V^2 [37] and replacing it into the aforementioned Jackson–Hunt expression, the resulting expression for λ can be expressed as a function of $\dot{T}^{-0.25}$. When the four examined alloys are compared, the proposed experimental equations show that the addition of Bi into the Zn–8 mass% Al alloy did not refine or thicken (λ_L) and (λ_F). Observing the graphs of Fig. 25, the profile of the fibrous spacing is about twice that of the lamellar spacing.

Bi droplets are derived from the solidification of the last liquid (L″) in the last invariant reaction, which refers to the eutectic reaction. As observed in Fig. 18, and as discussed in Sect. 3.2, a bimodal distribution [38, 39] of Bi droplets

can be observed, with the small droplets disseminated into the matrix formed by lamellae and fibers and larger droplets between the dendritic branches. It is worth noting that the diameter and distribution of these droplets are settled in the monotectic reaction since the Bi-rich liquid is trapped by the solidification monotectic front.

The determination of diameter and distribution of Bi droplets in the microstructure of the ternary alloys was carried out through the image processing ImageJ software. The dependence of the rate of displacement and of the cooling rate of the monotectic isotherm on the diameter and density of the fine Bi droplets/area is shown in Figs. 27 and 28, respectively. Comparing the ternary alloys, it can be observed that the increase in the Bi content of the alloy does not interfere with the dimensions of the fine droplets. Moreover, the distance between lamellae and fibers is also not affected by the addition of Bi, as shown in Figs. 25 and 26.

As discussed in the previous subsection, the presence of larger Bi droplets entrapped between the dendritic branches

can be observed only in the microstructures of the alloys containing 2.3 and 3 mass% of Bi, due to the displacement of the monotectic invariant point. As can be seen in Figs. 29 and 30, when the Bi content of the alloy increases from 2.3 to 3 mass%, the average diameter of the large Bi particles is not affected; however, a slight increase in the area distribution of these droplets can be observed.

Conclusions

The following conclusions can be drawn from the present experimental investigation:

- The microstructure of the directionally solidified (DS) Zn–8 mass% Al alloy was shown to be formed at the eutectic temperature by the eutectic mixture [L↔(Al′)+(Zn)] and equiaxed dendrites of the (Al′) phase. With the subsequent cooling, a eutectoid transformation occurs [(Al′)↔(Al)+(Zn)] both within the eutectic mixture and in the dendritic (Al′) phase, resulting in a microstructure characterized by equiaxed dendrites disseminated into an (Al)/(Zn) lamellar matrix.

- The cooling from the melt of Zn–8 mass% Al–XBi ($X=$ 1.5, 2.3 and 3 mass%) alloys was shown to be characterized by three invariant reactions, that is, a monotectic [L′↔L″+(Al′)+(Zn)], followed by a eutectoid [(Al)′+(Zn)+L″↔(Al)+(Zn)+L″] and finally by a eutectic reaction [(L″)↔(Al)+(Zn)+(Bi)] leading to the solidification of the Bi particles. However, the microstructural phases of the ternary alloys are quite similar to that of the binary alloy, with equiaxed dendrites immersed in a matrix consisting of the Al/Zn eutectoid product in the form of fibers or lamellae. The microstructures of the ternary alloys differ from the binary one basically by the presence of Bi droplets. For the alloys having higher Bi content, a bimodal distribution of Bi droplets was shown to occur, with the small droplets disseminated into the matrix consisting of lamellae and fibers, and larger droplets between the dendritic branches.

- Experimental expressions relating the secondary dendritic arm spacing, λ_2, the spacing between lamellae, λ_L, and the fiber spacing, λ_F, to the solidification thermal parameters have been derived. The evolution of λ_2 as a function of the rate of displacement of the liquidus isotherm (V_L) and the corresponding cooling rate ($\dot{T}_L$) was shown to be given for all examined alloys by:

$$\lambda_2 = 7.5 \, V_L^{-2/3} \text{ and } \lambda_2 = 15 \, \dot{T}_L^{-1/3}$$

The experimental microstructural spacings (λ_L) and (λ_F) along the length of the DS castings were shown to be related to the rates of displacement of the eutectic isotherm (V_E) for the binary alloy and of the monotectic isotherm (V_M) for the ternary alloys, as well as to the cooling rates ahead of these isotherms ($\dot{T}_E$ e $\dot{T}_M$), by the following expressions:

$$\lambda_L = 0.34 \, V_{E/M}^{-1/2} \text{ and } \lambda_F = 0.60 \, V_{E/M}^{-1/2}$$
$$\lambda_L = 0.75 \, \dot{T}_{E/M}^{-1/4} \text{ and } \lambda_F = 1.39 \, \dot{T}_{E/M}^{-1/4}$$

where, $\lambda_{2/L/F}$ (µm); $V_{L/E/M}$ (mm s^{-1}) and $\dot{T}_{L/E/M}$ (°C s^{-1}).

- The diameter and distribution of fine Bi droplets along the length of the DS ternary alloys castings were shown to be essentially constants, i.e., they are not significantly affected by V_M or $\dot{T}_M$. Moreover, the increase in the Bi content of the alloy was shown not to interfere with the dimensions of the fine droplets. In contrast, the diameter of the large Bi droplets decreased with the increase in V_M or $\dot{T}_M$.

References

1. Türk A, Kurnaz C, Şevik H. Comparison of the wear properties of modified ZA-8 alloys and conventional bearing bronze. Mater Des. 2007;28:1889–97.

2. Şevik H. The effect of silver on wear behaviour of zinc–aluminium-based ZA-12 alloy produced by gravity casting. Mater Charact. 2014;89:81–7.

3. Pola A, Montesano L, Gelfi M, La Vecchia GM. Comparison of the sliding wear of a novel Zn alloy with that of two commercial Zn alloys against bearing steel and leaded brass. Wear. 2016;368–369:445–52.

4. Silva BL, Cheung N, Garcia A, Spinelli JE. Thermal parameters, microstructure, and mechanical properties of directionally solidified Sn–0.7 wt% Cu solder alloys containing 0 ppm to 1000 ppm Ni. J Electron Mater. 2013;42:179–91.

5. Bertelli F, Brito C, Ferreira IL, Reinhart G, Nguyen-Thi H, Mangelinck-Noël N, Cheung N, Garcia A. Cooling thermal parameters, microstructure, segregation and hardness in directionally solidified Al–Sn–(Si;Cu) alloys. Mater Des. 2015;72:31–42.

6. Altıntas Y, Öztürk E, Aksöz S, Keşlioğlu K, Maraşlı N. Thermal conductivity and interfacial energy of solid Bi in the Bi–Ag eutectic system. J Therm Anal Calorim. 2015;122:65–72.

7. Şahin M, Şensoy T, Çadırlı E. Microstructural evolution and mechanical properties of Sn–Bi–Cu ternary eutectic alloy produced by directional solidification. Mater Res. 2018;21:e20170901.

8. Şahin M, Çadırlı E, Bayram Ü, Ata Esener P. Investigation of the thermoelectrical properties of the Sn$_{91.2-x}$–Zn$_{8.8}$–Ag$_x$ alloys. J Therm Anal Calorim. 2018;132:317–32.

9. Osório WR, Santos CA, Quaresma JMV, Garcia A. Mechanical properties as a function of thermal parameters and microstructure of Zn–Al castings. J Mater Process Technol. 2003;143:703–9.
10. Santos GA, Moura Neto C, Osório WR, Garcia A. Design of mechanical properties of a Zn27Al alloy based on microstructure dendritic array spacing. Mater Des. 2007;28:2425–30.
11. Pizarro-Pastene M, Fornaro O, Medina HO. Study of directional solidification of Zn–Al alloys. Proc Mater Sci. 2012;1:87–94.
12. Savaşkan T, Turhal MŞ. Relationships between cooling rate, copper content and mechanical properties of monotectoid based Zn–Al–Cu alloys. Mater Charact. 2003;51:259–70.
13. Yan SQ. Microstructures and mechanical properties of Zn–Al Alloy with addition of different Si morphologies. Metallogr Microstruct Anal. 2014;3:213–8.
14. Modi OP, Rathod S, Prasad BK, Jha AK, Dixit G. The influence of alumina particle dispersion and test parameters on dry sliding wear behaviour of zinc-based alloy. Tribol Int. 2007;40:1137–46.
15. Phanikumar G, Dutta P, Galun R, Chattopadhyay K. Microstructural evolution during remelting of laser surface alloyed hyper-monotectic Al–Bi alloy. Mater Sci Eng A - Struct. 2004;371:91–102.
16. Kamio A, Kumai S, Tezuka H. Solidification structure of monotectic alloys. Mater Sci Eng A - Struct. 1991;146:105–21.
17. Kaban I, Köhler M, Ratke L, Nowak R, Sobczak N, Mattern N, Eckert J, Greer AL, Sohn SW, Kim DH. Phase separation in monotectic alloys as a route for liquid state fabrication of composite materials. J Mater Sci. 2012;47:8360–6.
18. Zhao JZ, He J, Hu ZQ, Ratke L. Microstructure evolution in immiscible alloys during rapid directional solidification. Z Met. 2004;95:362–8.
19. Gröbner J, Mirković D, Schmid-Fetzer R. Monotectic four-phase reaction in Al–Bi–Zn alloys. Acta Mater. 2005;53:3271–80.
20. Gröbner J, Schmid-Fetzer R. Phase transformations in ternary monotectic aluminum alloys. JOM. 2005;57:19–23.
21. Mirković D, Gröbner J, Schmid-Fetzer R. Solidification paths of multicomponent monotectic aluminum alloys. Acta Mater. 2008;56:5214–22.
22. Costa TA, Freitas ES, Dias M, Brito C, Cheung N, Garcia A. Monotectic Al–Bi–Sn alloys directionally solidified: effects of Bi content, growth rate and cooling rate on the microstructural evolution and hardness. J Alloys Compd. 2015;653:243–54.
23. Zheng H, Ma W, Zheng C, Guo X, Li J. Rapid solidification of undercooled monotectic alloy melts. Mater Sci Eng A - Struct. 2003;355:7–13.
24. Günduz M, Çadırlı E. Directional solidification of aluminium–copper alloys. Mater Sci Eng A - Struct. 2002;327:167–85.
25. Çadırlı E, Marasli N, Bayender B, Gündüz M. Dependency of the microstructure parameters on the solidification parameters for camphene. Mater Res Bull. 2000;35(6):985–95.
26. Ratke L, Diefenbach S. Liquid immiscible alloys. Mater Sci Eng, R. 1996;19:263–347.
27. Cao C, Chen L, Xu J, Zhao J, Pozuelo M, Li X. Phase control in immiscible Zn–Bi alloy by tungsten nanoparticles. Mater Lett. 2016;174:213–6.
28. http://www.matweb.com. Accessed 20 Apr 2019.
29. Murray JL. The Al–Zn (aluminum-zinc) system. Bull Alloy Phase Diagr. 1983;4:55–73.
30. Raghavan V. Al–Bi–Zn (aluminum–bismuth–zinc). J Phase Equilib Diffus. 2008;29:167–8.
31. Zhu YH. General rule of phase decomposition in Zn–Al based alloys (II). Mater Trans. 2004;45:3083–97.
32. Bluni ST, Notis MR, Marder AR. Nucleation characteristics and microstructure in off-eutectic Al–Zn alloys. Acta Met Mater. 1995;43:1775–82.
33. Yang W, Fredriksson H, Ji S. Halo formation of Zn–Al alloys under conventional solidification and intensive convection solidification. J Alloys Compd. 2017;696:460–9.
34. Souza EN, Cheung N, Garcia A. The correlation between thermal variables and secondary dendrite arm spacing during solidification of horizontal cylinders of Sn–Pb alloys. J Alloys Compd. 2005;399:110–7.
35. Castanho MAP, Goulart PR, Brito C, Spinelli JE, Cheung N, Garcia A. Steady and unsteady state peritectic solidification. Mater Sci Technol. 2015;31:105–14.
36. Canté MV, Spinelli JE, Ferreira IL, Cheung N, Garcia A. Microstructural development in Al–Ni alloys directionally solidified under unsteady-state conditions. Metall Mater Trans A. 2008;39:1712–26.
37. Garcia A, Prates M. Mathematical model for the unidirectional solidification of metals: I. Cooled molds. Metall Trans B. 1978;9:449–57.
38. Chakrabarti D, Davis C, Strangwood M. Characterisation of bimodal grain structures in HSLA steels. Mater Character. 2007;58:423–38.
39. Kakitani R, Reyes RV, Garcia A, Spinelli JE, Cheung N. Relationship between spacing of eutectic colonies and tensile properties of transient directionally solidified Al–Ni eutectic alloy. J Alloys Compd. 2018;733:59–68.

Publisher's Note Springer Nature remains neutral with regard to jurisdictional claims in published maps and institutional affiliations.

Affiliations

Rudimylla S. Septimio[1] · Thiago A. Costa[2] · Cássio A. P. Silva[3] · Talita A. Vida[4] · Juan de Damborenea[5] · Amauri Garcia[4] · Noé Cheung[4]

✉ Noé Cheung
cheung@fem.unicamp.br

1 Institute of Geosciences and Engineering, Federal University of the South and Southeast of Pará, UNIFESSPA, Marabá, PA 68050-080, Brazil

2 Federal Institute of Education, Science and Technology of Pará, IFPA, Belém, PA 66093-020, Brazil

3 Federal University of São Paulo, UNIFESP, São José dos Campos, SP 12231-280, Brazil

4 Department of Manufacturing and Materials Engineering, University of Campinas, UNICAMP, Campinas, SP 13083-860, Brazil

5 National Center for Metallurgical Research, CENIM-CSIC, 28040 Madrid, Spain